

1 **WHAMM functions in kidney reabsorption and polymerizes actin to**  
2 **promote autophagosomal membrane closure and cargo sequestration**

3

4 Running Title: WHAMM in kidney function and autophagy

5

6 **Alyssa M Coulter<sup>1=</sup>, Valerie Cortés<sup>2=</sup>, Corey J Theodore<sup>1</sup>, Rachel E Cianciolo<sup>3</sup>, Ron**  
7 **Korstanje<sup>2\*</sup>, and Kenneth G Campellone<sup>1,4\*</sup>**

8

9 <sup>1</sup> Department of Molecular & Cell Biology, Institute for Systems Genomics; University of  
10 Connecticut, Storrs CT, USA.

11 <sup>2</sup> The Jackson Laboratory, Bar Harbor ME, USA.

12 <sup>3</sup> Niche Diagnostics LLC, Columbus OH, USA.

13 <sup>4</sup> Center on Aging; UConn Health, Farmington CT, USA

14

15

16 <sup>=</sup> Equal contributions

17 <sup>\*</sup> For correspondence:

18 Email: [ron.korstanje@jax.org](mailto:ron.korstanje@jax.org)

19 Email: [kenneth.campellone@uconn.edu](mailto:kenneth.campellone@uconn.edu)

20

21 **ABSTRACT**

22 The actin cytoskeleton is essential for many functions of eukaryotic cells, but the factors that  
23 nucleate actin assembly are not well understood at the organismal level or in the context of  
24 disease. To explore the function of the actin nucleation factor WHAMM in mice, we examined  
25 how *Whamm* inactivation impacts kidney physiology and cellular proteostasis. We show that  
26 male WHAMM knockout mice excrete elevated levels of albumin, glucose, phosphate, and  
27 amino acids, and display abnormalities of the kidney proximal tubule, suggesting that WHAMM  
28 activity is important for nutrient reabsorption. In kidney tissue, the loss of WHAMM results in the  
29 accumulation of the lipidated autophagosomal membrane protein LC3, indicating an alteration in  
30 autophagy. In mouse fibroblasts and human proximal tubule cells, WHAMM and its binding  
31 partner the Arp2/3 complex control autophagic membrane closure and cargo receptor  
32 recruitment. These results reveal a role for WHAMM-mediated actin assembly in maintaining  
33 kidney function and promoting proper autophagosome membrane remodeling.

## 43 INTRODUCTION

44 The actin cytoskeleton is crucial for controlling intracellular organization and the dynamics of  
45 membrane-bound organelles. To coordinate such cellular functions, globular (G-) actin  
46 monomers assemble into filamentous (F-) actin polymers (Pollard, 2016). Actin assembly is  
47 important in nearly all animal cells and tissues, although distinct physiological systems may rely  
48 on different regulatory factors (Rivers and Thrasher, 2017; Molinie and Gautreau, 2018;  
49 Kounakis and Tavernarakis, 2019). Despite this progress in understanding cytoskeletal  
50 activities, direct connections between dysfunctional actin assembly pathways and the  
51 pathogenesis of specific diseases are not well characterized.

52 To ensure that actin assembles when and where it is needed, proteins called nucleators  
53 direct the initiation of actin polymerization (Rottner *et al.*, 2017; Gautreau *et al.*, 2021). In  
54 mammals, these include a nucleator called the Arp2/3 complex, which cooperates with ~12  
55 activators, termed nucleation-promoting factors (Campellone and Welch, 2010). Most Arp2/3  
56 activators are members of the Wiskott-Aldrich Syndrome Protein (WASP) family (Alekhina *et al.*,  
57 2017; Kabrawala *et al.*, 2020). The WASP, WAVE, and WASH subgroups within the family have  
58 been thoroughly studied during plasma membrane dynamics, cell migration, and endocytic  
59 trafficking (Kramer *et al.*, 2022). In contrast, the activities of the WHAMM/JMY subgroup have  
60 emerged in processes that were overlooked for many years (Campellone *et al.*, 2023). WHAMM  
61 was discovered to promote ER-Golgi transport, endomembrane tubulation, and actin-  
62 microtubule interactions (Campellone *et al.*, 2008; Shen *et al.*, 2012; Russo *et al.*, 2016), while  
63 JMY was recognized for roles in gene expression, motility, and *trans*-Golgi transport (Shikama  
64 *et al.*, 1999; Zuchero *et al.*, 2009; Schluter *et al.*, 2014). More recent studies have revealed that  
65 WHAMM and JMY both function in autophagy and apoptosis (Coutts and La Thangue, 2015;  
66 Kast *et al.*, 2015; Mathiowetz *et al.*, 2017; Dai *et al.*, 2019; Hu and Mullins, 2019; King *et al.*,  
67 2021; Wu *et al.*, 2021). Although the activities of these two factors in apoptosis appear to lie in

68 cytosolic actin rearrangements (King *et al.*, 2021; King and Campellone, 2023), their  
69 participation in autophagy involves organelle remodeling.

70 Autophagy (formally, macroautophagy) is a mechanism of cytoplasmic digestion wherein  
71 double membrane-bound organelles called autophagosomes engulf cytoplasmic material and  
72 fuse with lysosomes for degradation (Zhao and Zhang, 2019; Vargas *et al.*, 2023). This process  
73 is crucial for organismal development and cellular homeostasis and takes place constitutively,  
74 but is also induced by nutrient starvation, proteotoxic stress, and other stimuli (Dikic and Elazar,  
75 2018; Levine and Kroemer, 2019). During autophagosome biogenesis, PI(3)P-rich phagophore  
76 membranes surround cytoplasmic cargo (Axe *et al.*, 2008; Devereaux *et al.*, 2013; Mi *et al.*,  
77 2015). This activity involves the ATG8 family of proteins, including the mammalian LC3s  
78 (LC3A/B/C) and GABARAPs (GABARAP, GABARAP-L1/L2), which exist as immature forms  
79 (e.g., LC3-I) that are cytosolic, and mature phosphatidylethanolamine-conjugated forms (e.g.,  
80 LC3-II) that are physically linked to autophagosomal membranes (Mizushima, 2020; Klionsky *et al.*  
81 *et al.*, 2021). Selective autophagy receptors, such as SQSTM1/p62, act as adaptors by binding  
82 both to LC3 and ubiquitinated cellular 'cargo' (Pankiv *et al.*, 2007; Johansen and Lamark, 2020;  
83 Vargas *et al.*, 2023). Autophagic flux takes place upon syntaxin-mediated autophagosome  
84 fusion with lysosomes and the degradation and recycling of macromolecules (Nakamura and  
85 Yoshimori, 2017). Following autolysosomal membrane tubulation, lysosomes can be  
86 regenerated, enabling them to maintain cellular proteostasis (Ballabio and Bonifacino, 2020).

87 A specific function for actin dynamics in autophagy was initially revealed when the  
88 interiors of phagophores were found to be shaped by actin assembly in a PI(3)P-dependent  
89 manner (Mi *et al.*, 2015). Subsequently, WHAMM and JMY were shown to act at multiple steps  
90 in the canonical autophagy pathway. WHAMM binds to PI(3)P, localizes to subdomains of  
91 nascent autophagosomes, and is important for efficient LC3 lipidation (Mathiowetz *et al.*, 2017).  
92 WHAMM-driven Arp2/3 activation also increases the size of autophagosomes and causes actin-  
93 based rocketing in the cytosol (Kast *et al.*, 2015). JMY binds LC3 and affects autophagosome

94 maturation (Coutts and La Thangue, 2015). Upon activation by LC3, JMY additionally promotes  
95 actin-based autophagosome rocketing (Hu and Mullins, 2019). WHAMM participates again later  
96 in the autophagy pathway by binding PI(4,5)P<sub>2</sub> and mediating autolysosome tubulation (Dai *et*  
97 *al.*, 2019; Wu *et al.*, 2021). WHAMM function is ultimately important for the degradation of p62  
98 and turnover of ubiquitinated cargo (Mathiowetz *et al.*, 2017).

99         Although the founding member of the WASP family was discovered due to genetic  
100 mutations in patients with immunodeficiencies decades ago (Derry *et al.*, 1994), surprisingly  
101 little is understood about how alterations in other family members contribute to disease. Several  
102 mutant versions of WAVE- or WASH-binding proteins have been observed in individuals with  
103 neurological or immunological disorders (Kramer *et al.*, 2022; Campellone *et al.*, 2023), but  
104 mutations in the WASP-family genes themselves are only beginning to be characterized  
105 (Valdmanis *et al.*, 2007; Ropers *et al.*, 2011; Ito *et al.*, 2018; Courtland *et al.*, 2021; Srivastava  
106 *et al.*, 2021). *WHAMM* variants play a potential role in disease, as most Amish patients with the  
107 rare neurodevelopmental/kidney disorder Galloway-Mowat Syndrome (GMS) harbor a  
108 homozygous *WHAMM* mutation that abrogates WHAMM-driven Arp2/3 activation *in vitro* and  
109 leads to autophagy defects in cells (Jinks *et al.*, 2015; Mathiowetz *et al.*, 2017). However, GMS  
110 has a complex genetic basis, as Amish patients also possess a homozygous mutation in the  
111 nearby *WDR73* gene which is considered to be disease-causing (Jinks *et al.*, 2015). *WDR73*  
112 mutations are associated with multiple neurological illnesses (Colin *et al.*, 2014; Ben-Omran *et*  
113 *al.*, 2015; Vodopituz *et al.*, 2015; Jiang *et al.*, 2017; El Younsi *et al.*, 2019; Tilley *et al.*, 2021),  
114 and loss-of-function mutations in many different genes can give rise to GMS or GMS-like  
115 conditions (Braun *et al.*, 2017; Rosti *et al.*, 2017; Braun *et al.*, 2018; Arrondel *et al.*, 2019; Mann  
116 *et al.*, 2021). Thus, the contribution of WHAMM to health and disease is difficult to discern. In  
117 the current study, we generated a null mutation in mouse *Whamm* to better define its role in  
118 kidney physiology and cellular autophagy.

## 119 RESULTS

### 120 WHAMM knockout male mice display proximal tubule reabsorption defects

121 To understand the organismal function of WHAMM, we used a *Whamm* allele with a targeted  
122 deletion in exon 3 to generate homozygous WHAMM knockout (WHAMM<sup>KO</sup>) mice (Figure 1A).  
123 We then compared the mutant mice to wild type (WHAMM<sup>WT</sup>) littermates in multiple phenotypic  
124 analyses. Since Amish GMS patients have kidney abnormalities resulting in proteinuria (Jinks *et*  
125 *al.*, 2015), we tested the urine from wild type and knockout mice for albuminuria. WHAMM<sup>KO</sup>  
126 males displayed a significant increase in the albumin-to-creatinine ratio (ACR) compared to  
127 WHAMM<sup>WT</sup> males at 24 weeks-of-age (Figure 1B). In contrast, ACRs for KO and WT females  
128 were statistically indistinguishable from one another (Figure 1B). To determine the age of onset  
129 for male albuminuria, we compared the ACRs at 16, 20, and 24-week timepoints. While  
130 WHAMM<sup>WT</sup> males showed a slight decrease in ACR over time, WHAMM<sup>KO</sup> males showed a  
131 gradual increase in ACR, although a statistically significant difference between the WT and KO  
132 was not reached until 24 weeks (Supplemental Figure S1).

133 To explore whether the inactivation of *Whamm* affected other parameters of kidney  
134 function, we next analyzed urinary glucose levels. WHAMM<sup>KO</sup> male mice displayed significantly  
135 higher glucose-to-creatinine ratios (GCR) at 20 and 24 weeks-of-age (Figure 1C). This  
136 phenotype was also sex-specific, as knockout and wild type females were similar to one another  
137 (Supplemental Figure S1). The urinary excretion of glucose in males did not appear to be  
138 caused by diabetes, as non-fasting plasma glucose levels did not differ between the KO and WT  
139 (Figure 1D).

140 Given the potential loss of multiple molecules in urine, we additionally measured urinary  
141 phosphate, potassium, sodium, chloride, and calcium in the 24-week-old males. The WHAMM<sup>KO</sup>  
142 mice had a significantly higher urinary phosphate-to-creatinine ratio (PhosCR) and potassium-  
143 to-creatinine ratio (KCR) than the WHAMM<sup>WT</sup> mice, whereas urinary sodium (NaCR), chloride  
144 (ClCR), and calcium (CaCR) did not show differences between the two genotypes of male mice

145 (Figure 1E). Because glucose, phosphate, and potassium are reabsorbed from the filtrate in the  
146 proximal tubule, these results are indicative of a tubular malfunction in the WHAMM<sup>KO</sup> males.

147 Notably, the WHAMM<sup>KO</sup> excretion phenotypes are reminiscent of those found in renal  
148 Fanconi Syndromes, proximal tubule diseases with diverse genetic bases ([Klootwijk et al., 2015](#);  
149 [Lemaire, 2021](#)). As amino aciduria is also seen in Fanconi Syndromes, we used mass  
150 spectrometry to measure the relative levels of different amino acids in the urine of 24-week-old  
151 knockout and wild type males. The WHAMM<sup>KO</sup> males showed statistically significant increases  
152 in urinary glutamic acid, glutamine, methionine, pipercolic acid, proline, and cysteine (Figure 2).  
153 These results further support the conclusion that WHAMM deficiency causes a Fanconi-like  
154 Syndrome in male mice.

155

#### 156 **WHAMM deletion alters proximal tubule polarity in male kidneys**

157 Previous work has shown that WHAMM protein is abundant in the human and mouse kidney  
158 ([Campellone et al., 2008](#)), but the more precise locations of its expression in the nephron have  
159 not been described. To assess the cell type-specific mRNA expression pattern of *Whamm*, we  
160 surveyed single-cell sequencing data from male and female adult mouse kidneys ([Ransick et](#)  
161 [al., 2019](#)). *Whamm* mRNA was present throughout the proximal tubule of both male and female  
162 mice, with its highest expression found in segment 2 of the proximal tubule of male mice  
163 (Supplemental Figure S2). *Whamm* levels in the proximal tubule were higher than those in  
164 podocytes but less than those in intercalated type-B cells of the cortical collecting duct  
165 (Supplemental Figure S2). Analyses of *Whamm* and other WASP-family and Arp2/3 complex  
166 genes indicated that they were all expressed in podocytes and proximal tubules to varying  
167 degrees, with the exceptions of *Was* (encoding WASP), *Wasf1* (WAVE1), and *Actr3b* (the  
168 Arp3B isoform), which were absent (Supplemental Figure S3). WHAMM expression in the  
169 proximal tubule of male mice is therefore amenable to a role in tubular reabsorption.

170 Some proximal tubule disorders have been attributed to endocytic trafficking defects and

171 reductions in the quantities of receptor proteins (Norden *et al.*, 2002; Oltrabella *et al.*, 2015;  
172 Inoue *et al.*, 2017; Festa *et al.*, 2019; Berquez *et al.*, 2020; Lemaire, 2021). Given that the  
173 physiological abnormalities in WHAMM-deficient mice were sex-specific, we focused our efforts  
174 on characterizing tissues and cells from males. To assess the amounts of the multiligand  
175 endocytic receptor LRP2/Megalin, the tubule-expressed angiotensin-converting enzyme ACE2,  
176 the glucose transporter SGLT2, and the phosphate transporter SLC20A1 in WHAMM<sup>WT</sup> and  
177 WHAMM<sup>KO</sup> males, we isolated their kidneys and generated tissue extracts for immunoblotting.  
178 While Megalin levels were highly variable, especially in the knockouts, the relative amount of  
179 each receptor protein was generally similar in WHAMM<sup>WT</sup> and WHAMM<sup>KO</sup> kidney tissue  
180 (Supplemental Figure S4), suggesting that WHAMM deficiency does not dramatically alter the  
181 abundance of membrane receptors in the kidney.

182 To provide a broad appraisal of kidney structure in the mice, we performed histological  
183 analyses of kidney sections after periodic acid-Schiff (PAS) staining, but did not observe any  
184 major differences between samples from male WHAMM<sup>WT</sup> and WHAMM<sup>KO</sup> animals (all slides  
185 can be viewed at <https://images.jax.org/webclient/?show=dataset-2763>). To more specifically  
186 visualize proximal tubule morphology and polarity, we stained kidney sections from WHAMM<sup>WT</sup>  
187 and WHAMM<sup>KO</sup> males with fluorescent antibodies to Megalin and ACE2 (Figure 3A;  
188 Supplemental Figure S5), as both proteins are expected to localize to the apical regions of  
189 proximal tubule cells (Kerjaschki *et al.*, 1984; Warner *et al.*, 2005).

190 In accordance with the earlier immunoblotting results, measurements of the  
191 immunofluorescence intensities of Megalin and ACE2 revealed that wild type and knockout  
192 males contained similar amounts of each protein per cluster of tubular cells (Figure 3B;  
193 Supplemental Figure S5). However, close inspection of the localization of each protein revealed  
194 several differences. Megalin immunostaining was quite variable, but exhibited a primarily apical  
195 localization in most WHAMM<sup>WT</sup> samples (Supplemental Figure S5). In WHAMM<sup>KO</sup> samples,  
196 tubular clusters looked more disorganized and sometimes displayed a Megalin staining pattern



197 that was less apical and more cytoplasmic (Supplemental Figure S5). For ACE2, staining was  
198 consistently apical in WT kidney sections but strikingly cytoplasmic in the KO sections (Figure  
199 3A). Quantification of apical and cytoplasmic ACE2 intensity across many tubule clusters in  
200 multiple animals demonstrated that ACE2 displayed an apical-to-cytoplasmic polarity ratio of 3:1  
201 in WHAMM<sup>WT</sup> samples but that the polarity ratio fell to nearly 1:1 for the WHAMM<sup>KO</sup> (Figure 3C).  
202 A defect in polarized receptor distribution was further confirmed using fluorescence linescan  
203 analyses, which showed sharp peaks of apical ACE2 intensity in WHAMM<sup>WT</sup> kidneys but a  
204 muted apical ACE2 localization WHAMM<sup>KO</sup> kidneys (Figure 3D). Together, our kidney tissue  
205 immunoblotting and immunofluorescence data demonstrate that while receptor abundance is  
206 relatively normal across both genotypes of male mice, the organization within proximal tubule  
207 cells appears to be distorted in the absence of WHAMM.

208

### 209 **The lipidation status of the autophagosomal protein LC3 is altered in WHAMM<sup>KO</sup> kidneys**

210 Cellular proteostasis systems are important for maintaining the integrity of proximal tubules  
211 (Cybulsky, 2017; Tang *et al.*, 2020), and conditional deletions of Vps34, a key initiator of  
212 autophagic membrane biogenesis, alter the urinary proteome and perturb the apical localization  
213 of several membrane transport proteins including ACE2 in mice (Grieco *et al.*, 2018; Rinschen  
214 *et al.*, 2022). Because WHAMM plays a role in multiple steps of autophagy (Kast *et al.*, 2015;  
215 Mathiowetz *et al.*, 2017; Dai *et al.*, 2019; Wu *et al.*, 2021), we next sought to determine whether  
216 some aspect of autophagy might be altered in WHAMM<sup>KO</sup> kidney tissue. The LC3 and  
217 GABARAP families of proteins are the most widely accepted markers of autophagosomal  
218 membranes, and LC3-II and GABARAP-II levels are considered to correlate with  
219 autophagosome quantities (Klionsky *et al.*, 2021), so we immunoblotted kidney extracts with  
220 polyclonal antibodies that recognize both the immature and mature species of multiple LC3 and  
221 GABARAP isoforms.

222 In male kidneys, immature LC3-I and GABARAP-I levels appeared similar across both  
223 WHAMM genotypes (Figure 4A). However, mature lipidated LC3-II was more abundant in  
224 WHAMM<sup>KO</sup> than WHAMM<sup>WT</sup> kidney tissue (Figure 4A). None of the kidney extracts contained  
225 detectable levels of GABARAP-II (Figure 4A). Quantification of the LC3 species revealed that  
226 LC3-II was present, on average, in 3-fold higher amounts in the knockout than the wild type, and  
227 that the LC3 II:I ratio was also substantially greater in the KO males (Figure 4B). In female  
228 kidneys, LC3-II levels were not elevated. The only statistically significant difference between KO  
229 and WT females was in the LC3 II:I ratio, which was slightly reduced in the WHAMM<sup>KO</sup>  
230 (Supplemental Figure S6). Collectively, these results suggest that the lack of WHAMM leads to  
231 altered LC3 modification in the murine kidney, with males experiencing an increase in LC3  
232 lipidation and/or a decrease in LC3-II turnover.

233

#### 234 **The morphogenesis of autophagic membranes is controlled by WHAMM**

235 To better define the function of WHAMM at the cellular level, we next generated male WHAMM-  
236 proficient (WHAMM<sup>HET</sup>) and WHAMM-deficient (WHAMM<sup>KO</sup>) mouse embryonic fibroblasts  
237 (MEFs) (Supplemental Figure S7). WHAMM was initially characterized for its ability to activate  
238 Arp2/3 complex-dependent actin assembly, bind microtubules, and interact with membranes to  
239 promote anterograde transport (Campellone *et al.*, 2008), but F-actin, microtubule, and *cis*-Golgi  
240 organization was relatively normal in knockout MEFs under standard culture conditions  
241 (Supplemental Figure S7).

242 Given our findings that WHAMM-deficient mouse kidneys accumulated lipidated LC3, we  
243 examined how WHAMM deletion affected autophagy in MEFs. At steady state, MEFs displayed  
244 diffuse LC3 and GABARAP staining without any cytosolic puncta and with minimal differences  
245 between genotypes (Supplemental Figure S7). This could be the result of low basal levels of  
246 autophagy and/or high rates of autophagosome turnover in embryo-derived cells. Therefore, to  
247 visualize autophagic structures, we prevented lysosomal degradation by treating MEFs with

248 chloroquine. While WHAMM<sup>HET</sup> cells formed discrete cup-shaped and ring-like LC3- and  
249 GABARAP-positive structures reminiscent of autophagosomes, WHAMM<sup>KO</sup> cells showed more  
250 diffuse and small punctate LC3 and GABARAP staining patterns (Figure 5, A and B).  
251 Quantification of whole cell mean fluorescence intensities for LC3 and GABARAP demonstrated  
252 that the WHAMM deletion increased the intracellular abundance of both ATG8 subfamilies  
253 (Figure 5C). In addition, whereas actin localized to LC3- and GABARAP-labeled membranes in  
254 WHAMM<sup>HET</sup> MEFs, little actin was recruited to autophagosomes in WHAMM<sup>KO</sup> MEFs (Figure 5,  
255 A and B). These findings indicate that the permanent loss of WHAMM in MEFs causes defects  
256 in both actin assembly at and organization of LC3- and GABARAP-associated structures.

257 To determine if increasing the initiation of autophagy could also influence autophagic  
258 membrane morphology differentially in WHAMM-proficient versus WHAMM-deficient cells, we  
259 exposed MEFs to the autophagy-inducing mTOR inhibitor rapamycin. While neither WHAMM<sup>HET</sup>  
260 nor WHAMM<sup>KO</sup> cells displayed any discernible LC3-positive autophagosomes after rapamycin  
261 treatment, WHAMM<sup>HET</sup> cells formed several GABARAP puncta (Figure 5D). Quantification of the  
262 number of GABARAP puncta per cell and the puncta-to-cytoplasmic GABARAP intensity ratio  
263 revealed that, compared to WHAMM<sup>HET</sup> MEFs, WHAMM<sup>KO</sup> MEFs did not effectively shape  
264 GABARAP-associated autophagic membranes into discrete puncta (Figure 5D). Overall, the  
265 presence of disorganized LC3 and/or GABARAP structures in WHAMM<sup>KO</sup> MEFs demonstrates  
266 the importance of WHAMM in promoting autophagic membrane morphogenesis.

267

### 268 **WHAMM activates the Arp2/3 complex to promote actin assembly, proper LC3** 269 **organization, and cargo sequestration in proximal tubule cells**

270 While the experiments in MEFs add to the existing literature about WHAMM in autophagy, our *in*  
271 *vivo* studies point to the kidney proximal tubule as the tissue type in which WHAMM function is  
272 most crucial. Therefore, we next studied autophagosome morphogenesis in the HK-2 human  
273 proximal tubule cell line. To examine the effects of transient WHAMM depletion, we transfected

274 HK-2 cells with control siRNAs or two independent siRNAs targeting the WHAMM transcript.  
275 Immunoblotting of cell extracts verified WHAMM protein knockdowns (Figure 6A). Following  
276 treatment of transfected HK-2 cells with chloroquine, control cells displayed LC3-positive  
277 circular autophagic structures that were often associated with actin (Figure 6B). In contrast to  
278 these cells, but akin to the changes in LC3 morphology and actin assembly observed in  
279 WHAMM<sup>KO</sup> MEFs, WHAMM-depleted HK-2 cells exhibited disorganized LC3 staining and  
280 diffuse actin staining (Figure 6B). Linescans of LC3 structures in control cells showed strong  
281 actin recruitment at (Figure 6C, i), around (Figure 6C, ii), and within (Figure 6C, iii;  
282 Supplemental Figure S8) autophagic membrane vesicles, whereas WHAMM-depleted cells  
283 showed disorganized LC3 staining with little actin enrichment (Figure 6C). Thus, permanent  
284 WHAMM deletion in fibroblasts and transient WHAMM depletion in proximal tubule cells both  
285 hinder autophagic membrane morphogenesis.

286         Because the best-characterized molecular activity of WHAMM is to promote Arp2/3  
287 complex-mediated actin polymerization, we next asked whether the Arp2/3 complex impacted  
288 autophagosome abundance, localization, or morphology in HK-2 cells. We exposed cells to  
289 normal media or to media containing the pharmacological Arp2/3 inhibitor CK666, chloroquine,  
290 or CK666 plus chloroquine. Fluorescence microscopy revealed that at steady state, both control  
291 and CK666-treated cells exhibited diffuse LC3 staining with no noticeable mature autophagic  
292 structures (Figure 7A). Upon lysosomal inhibition with chloroquine, LC3-positive rings  
293 accumulated throughout the cytoplasm and often associated with actin (Figure 7B). The  
294 combination of chloroquine and CK666 also caused LC3-associated structures to accumulate,  
295 but in a smaller perinuclear region, with less circular morphologies, and with minimal recruitment  
296 of actin (Figure 7B). Quantification indicated that Arp2/3 inhibition significantly reduced the  
297 proportion of cells with mature, ring-shaped LC3-positive autophagosomes, the number of LC3  
298 rings per cell, and the amount of actin localizing at or near the autophagic membrane (Figure 7,

299 C and D). Hence, like WHAMM, the Arp2/3 complex is important for the proper formation of  
300 mature, properly-shaped autophagosomes.

301 If the irregular morphologies of LC3-associated membranes are incompatible with  
302 efficient autophagosome closure, then the localization of proteins involved in autophagosome-  
303 lysosome fusion should be altered. Syntaxin-17 (STX17) is a SNARE protein that mediates  
304 autophagosome closure and is important for subsequent lysosome fusion (Itakura *et al.*, 2012;  
305 Tsuboyama *et al.*, 2016). To examine STX17 localization in the presence and absence of  
306 Arp2/3 complex activity, we treated HK-2 cells with DMSO or CK666, inhibited lysosomes with  
307 chloroquine, and stained the cells with antibodies to STX17 and LC3 (Figure 7E). Over 80% of  
308 DMSO-treated cells possessed STX17-positive vesicles, and on average each cell had two  
309 such vesicles (Figure 7E and F). Arp2/3 inhibition reduced both the percentage of cells  
310 containing STX17-positive vesicles and the number of STX17-associated vesicles per cell, while  
311 the vesicles that were present appeared smaller (Figure 7E and F). These findings further  
312 support the conclusion that efficient autophagosome closure is reliant on the Arp2/3 complex.

313 In the canonical selective autophagy pathway, LC3-decorated membranes interact with  
314 autophagy receptors, which are physically linked to ubiquitinated cargo (Vargas *et al.*, 2023). So  
315 we next asked whether the steps of receptor-ubiquitin or receptor-LC3 interactions were  
316 influenced by the Arp2/3 complex. SQSTM1/p62, an autophagy receptor with a wide range of  
317 selective targets, has been shown to associate with ubiquitinated protein aggregates that are  
318 destined for autophagic degradation (Pankiv *et al.*, 2007; Sarraf *et al.*, 2020). We therefore  
319 induced the production of truncated proteins in HK-2 cells using puromycin and assessed the  
320 effects of Arp2/3 inhibition on the recruitment of p62 to ubiquitinated material. Puromycin  
321 caused the formation of bright foci of ubiquitinated proteins, and p62 localized to the ubiquitin  
322 foci in the absence or presence of CK666 (Supplemental Figure S9), indicating that Arp2/3  
323 inactivation does not prevent the association between ubiquitinated cargo and p62. To evaluate  
324 the effect of Arp2/3 inhibition on the step of receptor-LC3 engagement, we examined the

325 recruitment of p62 to LC3. As expected, p62 localized to LC3-positive ring-shaped  
326 autophagosomes when cells were treated with chloroquine (Figure 7G). In cells subjected to  
327 concurrent chloroquine and CK666 treatment, the disorganized LC3 structures often co-stained  
328 for p62 (Figure 7G). However, the Arp2/3-inhibited cells contained additional p62 puncta that  
329 were independent of LC3 (Figure 7G). These results suggest that autophagosomal membrane  
330 remodeling is coupled to cargo capture and that this process is inefficient without an active  
331 Arp2/3 complex.

332 To connect the observations that both WHAMM and the Arp2/3 complex impact actin  
333 assembly at autophagic membranes, we studied actin organization in HK-2 cells expressing a  
334 LAP (localization and affinity purification) tagged version of either wild type WHAMM or a mutant  
335 WHAMM lacking a critical Arp2/3-binding residue (WHAMM W807A) (Campellone *et al.*, 2008).  
336 As predicted, wild type WHAMM localized to LC3-positive structures, and actin was enriched  
337 around these autophagic membranes (Figure 8A). Similar to cells depleted of WHAMM (Figure  
338 6), cells expressing the WHAMM W807A mutant protein displayed more diffuse cytoplasmic  
339 LC3 staining (Figure 8A). In cases where small LC3 puncta were observed, the puncta  
340 associated with WHAMM W807A but lacked actin (Figure 8A). Together, these results show that  
341 WHAMM stimulates Arp2/3 complex-mediated actin assembly to control autophagic membrane  
342 morphogenesis and cargo sequestration.

## 343 DISCUSSION

344 Actin nucleation factors are important players in a variety of processes that are crucial for  
345 cellular function. However, their roles in organismal health and disease have been relatively  
346 understudied. Deletion of several WASP-family members, including N-WASP, WAVE2, and  
347 WASH, results in embryonic lethality in mice ([Snapper et al., 2001](#); [Yan et al., 2003](#); [Gomez et](#)  
348 [al., 2012](#); [Xia et al., 2013](#)), demonstrating the essentiality of these factors in mammalian  
349 development. Similar animal studies of WASP-family proteins from the WHAMM/JMY subgroup  
350 had not been previously explored, so we focused our investigation on the impact of WHAMM  
351 inactivation in mice. Here we establish the importance of WHAMM in kidney physiology *in vivo*  
352 and in autophagosome closure during cargo capture in proximal tubule cells.

353 The inherited neurodevelopmental and kidney disorder Galloway-Mowat Syndrome is  
354 associated with several different *WDR73* mutations ([Colin et al., 2014](#); [Ben-Omran et al., 2015](#);  
355 [Vodopituz et al., 2015](#); [Jiang et al., 2017](#); [El Younsi et al., 2019](#); [Tilley et al., 2021](#)), but in  
356 patients from Amish communities, 26 of 27 affected individuals were found to be doubly  
357 homozygous for loss-of-function mutations in both *WDR73* and *WHAMM*, with one *WHAMM*  
358 heterozygous individual presenting with neurological symptoms but lacking renal symptoms  
359 ([Jinks et al., 2015](#); [Mathiowetz et al., 2017](#)). Given the genotypic and phenotypic variability of  
360 GMS, the extent to which WHAMM inactivation might modify the clinical outcomes in Amish  
361 patients has been unclear. Our current study begins to untangle the complexities of Amish GMS  
362 by showing that a targeted mutation in *WHAMM* by itself can cause kidney dysfunction in mice.

363 An elevated urinary protein:creatinine ratio and end-stage renal disease affect the  
364 majority of Amish GMS patients ([Jinks et al., 2015](#)). Recently, a targeted deletion in mouse  
365 *Wdr73* was found to be embryonic lethal ([Li et al., 2022](#)). However, a conditional *Wdr73* deletion  
366 in podocytes, terminally differentiated cells required for filtration in the glomerulus, yielded live  
367 mice. Such animals did not have any detectable kidney phenotypes until chemically-induced  
368 glomerular injury caused albuminuria ([Li et al., 2022](#)). These results contrast the loss of

369 WHAMM in mice, which is not lethal, but results in male-specific excretion of a low molecular  
370 weight protein, multiple solutes, and amino acids in the urine. Thus, while the molecular and  
371 cellular basis of GMS pathogenesis still requires much investigation, our characterization of  
372 kidney abnormalities in WHAMM-deficient mice supports the idea that the Amish *WHAMM*  
373 mutation may be a modifier in the nephrotic aspects of GMS.

374 Earlier studies in mice indicated that the WASP-family member N-WASP is also  
375 important for kidney function ([Schell et al., 2013](#); [Schell et al., 2018](#)). N-WASP regulates Arp2/3-  
376 and actin-driven membrane protrusions in podocytes, and deletion of Arp3 increases urinary  
377 excretion of albumin ([Schell et al., 2018](#)). Our current studies with WHAMM knockout mice  
378 provide new evidence that the WASP family also contributes to kidney physiology in a different  
379 anatomical location, the proximal tubule, which is crucial for reabsorption of small molecules  
380 from the filtrate.

381 The excretion profiles observed in WHAMM-deficient mice are reminiscent of those in  
382 other proximal tubule disorders, collectively referred to as Fanconi Syndromes ([van der Wijst et](#)  
383 [al., 2019](#); [Lemaire, 2021](#)). Dent disease type II ([Hoopes et al., 2005](#); [Utsch et al., 2006](#)) and  
384 Lowe Syndrome ([Zhang et al., 1995](#); [Bockenbauer et al., 2008](#); [Mehta et al., 2014](#)) are X-linked  
385 Fanconi disorders caused by mutations in the *OCRL* gene. *OCRL* encodes a lipid phosphatase,  
386 and loss of its enzymatic activity results in the accumulation of PI(4,5)P<sub>2</sub>, which leads to defects  
387 in endosomal trafficking and autophagy ([Vicinanza et al., 2011](#); [De Leo et al., 2016](#); [Daste et al.,](#)  
388 [2017](#); [De Matteis et al., 2017](#)). Given the endocytic and receptor degradation anomalies  
389 identified in Lowe Syndrome cells, we tested whether the levels of reabsorption receptors were  
390 altered in WHAMM<sup>KO</sup> kidneys but found no gross changes in receptor abundance. However, the  
391 irregular distribution of ACE2 staining in WHAMM knockout tissue is suggestive of defects in  
392 proximal tubule organization, polarity, or membrane trafficking. Interestingly, alterations in the  
393 urinary proteome, proximal tubule reabsorption, and ACE2 localization have also been observed  
394 upon disruption of Vps34, a PI-3 kinase with critical roles in autophagosome biogenesis and



395 endocytic trafficking (Grieco *et al.*, 2018; Rinschen *et al.*, 2022).

396 WHAMM was first studied for its functions in microtubule binding, anterograde transport,  
397 and Golgi morphogenesis (Campellone *et al.*, 2008), but stainings of WHAMM<sup>KO</sup> MEFs  
398 indicated that microtubule and Golgi organization were relatively normal. Taken together with  
399 the observations that Amish GMS patient cells have more dramatic defects in autophagosomes  
400 than secretory organelles (Mathiowetz *et al.*, 2017), we focused our attention on autophagy.  
401 Previous localization and loss-of-function approaches in human epithelial cells, fibroblasts,  
402 monkey kidney cells, and GMS patient samples demonstrated the importance of WHAMM early  
403 in autophagy during the steps of autophagosome biogenesis, enlargement, and movement  
404 (Kast *et al.*, 2015; Mathiowetz *et al.*, 2017). Additional work in human and rat kidney cell lines  
405 showed that WHAMM also plays a role later in autophagy by promoting autolysosome tubulation  
406 and turnover (Dai *et al.*, 2019; Wu *et al.*, 2021).

407 Our current study evaluated several autophagy-related parameters in mouse kidneys,  
408 mouse fibroblasts, and human proximal tubule cells to link the physiological dysfunction *in vivo*  
409 with alterations in autophagy *in vitro*. Higher levels of lipidated LC3 in male WHAMM<sup>KO</sup> kidney  
410 tissue first suggested that changes in autophagy accompanied the deficiencies in reabsorption.  
411 Fibroblasts generated from WHAMM-proficient or knockout mouse embryos next demonstrated  
412 that permanent WHAMM deletion not only resulted in higher overall cellular levels of the LC3  
413 and GABARAP classes of ATG8-family proteins, but also caused aberrations in  
414 autophagosomal membrane morphology and a reduction in actin recruitment. In proximal tubule  
415 cells, WHAMM and its actin nucleating binding partner, the Arp2/3 complex, were also crucial  
416 for the proper morphogenesis and closure of LC3-associated autophagosomes. These results  
417 give rise to a model in which WHAMM activates Arp2/3-mediated actin assembly to shape  
418 autophagosomal membranes in such a way that allows them to effectively capture autophagy  
419 receptors like p62 (Figure 8B). Without WHAMM or the Arp2/3 complex, receptor sequestration  
420 becomes inefficient, and the incompletely-sealed misshapen LC3-associated membranes

421 accumulate because their subsequent fusion with lysosomes is impaired.

422           The numerous functions of WHAMM throughout the autophagy pathway are likely  
423 coordinated based on the expression profiles of other proteins that regulate the initiation and  
424 progression of multiple degradation pathways. Genetically programmed, epigenetically  
425 modulated, or even stochastic changes in such regulatory factors probably determine when and  
426 where WHAMM function is most important in a particular cell type. Moreover, different  
427 compensatory changes that occur when WHAMM is permanently deleted versus transiently  
428 depleted add an additional layer of complexity to deciphering its usual cellular responsibilities.  
429 The complicated nature of mammalian protein homeostasis systems and their many potential  
430 connections to the actin assembly machinery are underscored by diversity in the repertoires of  
431 the (6) LC3/GABARAP isoforms and the (5) basic autophagy receptors ([Lazarou et al., 2015](#);  
432 [Nguyen et al., 2016](#)), and perhaps even in the WASP-family members (e.g., WHAMM and JMY)  
433 themselves. In the case of mice housed in standard laboratory conditions, the crucial functions  
434 for WHAMM appeared anatomically in the kidney proximal tubule and molecularly in  
435 LC3/GABARAP-associated autophagosome morphogenesis and closure.

436           The distinct excretion phenotypes in male versus female WHAMM<sup>KO</sup> mice, and the fact  
437 that tissue from only male knockouts showed substantial changes in LC3 lipidation, highlight a  
438 relationship between alterations in kidney function and molecular malfunctions in autophagy.  
439 The specific reasons for this male specificity are unclear, but other sex-specific discrepancies *in*  
440 *vivo* have been attributed to differences in the distribution and/or abundance of transporters  
441 throughout the nephron ([Veiras et al., 2017](#); [Harris et al., 2018](#); [Li et al., 2018](#); [Hu et al., 2020](#);  
442 [Torres-Pinzon et al., 2021](#)). Anatomically, males have a greater density of proximal tubules in  
443 the cortex, whereas in females the collecting duct comprises a larger volume ([Harris et al.,](#)  
444 [2018](#)). Modeling further suggests that a smaller transport area and varied expression of  
445 transporters results in less tubular reabsorption in females ([Li et al., 2018](#)). Autophagy rates  
446 also differ between males and females ([Shang et al., 2021](#)). Future work on the mechanisms

447 regulating autophagy in the proximal tubule is required to better understand the sex-based  
448 differences in kidney physiology arising from the loss of WHAMM.

449         Lowe Syndrome is X-linked, and excessive actin polymerization on multiple organelles is  
450 a prominent feature in cells from patients with this disorder ([Suchy and Nussbaum, 2002](#);  
451 [Vicinanza \*et al.\*, 2011](#); [Festa \*et al.\*, 2019](#); [Berquez \*et al.\*, 2020](#)). Alterations in PI(3)P and  
452 PI(4,5)P<sub>2</sub> membrane composition are key drivers of signaling to the actin nucleation machinery  
453 in this context, and N-WASP is at least partly responsible for the ectopic actin assembly  
454 ([Vicinanza \*et al.\*, 2011](#); [Daste \*et al.\*, 2017](#)). However, WHAMM is also capable of binding to  
455 PI(3)P ([Mathiowetz \*et al.\*, 2017](#)) and PI(4,5)P<sub>2</sub> ([Dai \*et al.\*, 2019](#)). So on one hand it is tempting  
456 to speculate that WHAMM-mediated Arp2/3 activation may influence the excess cytoskeletal  
457 rearrangements and trafficking modifications that take place in Lowe Syndrome cells, while on  
458 the other hand, reduced actin assembly may underlie the autophagy defects in WHAMM-  
459 depleted cells. This combination of previous data and our new findings are consistent with the  
460 idea that either over- or under-active actin assembly pathways can cause similar tubular  
461 reabsorption problems. Thus, proximal tubule function is governed by exquisitely tight  
462 spatiotemporal control of phospholipid signaling to the actin polymerization machinery. Future  
463 characterizations of the connections between key autophagy regulators and actin nucleation  
464 factors therefore hold promise for determining how proteostasis pathways and cytoskeletal  
465 activities collaborate in healthy kidneys and how their functions are altered during distinct  
466 diseases.

## 467 **MATERIALS AND METHODS**

### 468 **Mice**

469 A floxed *Whamm* allele generated by the Knockout Mouse Project (genome.gov/17515708)  
470 incorporated SA-IRES-*lacZ*-pA and *neo* cassettes between *Whamm* exons 2 and 3, with *loxP*  
471 sites located between the two cassettes and following exon 3. Cre-mediated recombination  
472 using the B6.C-Tg(CMV-Cre)1Cgn/J strain resulted in the excision of *neo* and exon 3, giving  
473 rise to a *Whamm* knockout allele. These B6N(Cg)-*Whamm*<sup>tm1b(KOMP)Wtsj</sup>/3J mice were obtained  
474 from The Jackson Laboratory (JAX stock JR#027472). Animals were maintained on pine  
475 shavings and given a standard rodent diet (LabDiet 5KOG) and acidified water in a pathogen-  
476 free room that was maintained at 21°C with a 12h light/dark cycle (6am to 6pm). Experimental  
477 animals were generated by mating heterozygous knockout (WHAMM<sup>HET</sup>) mice and selecting  
478 homozygous knockout (WHAMM<sup>KO</sup>) offspring and their wild type (WHAMM<sup>WT</sup>) littermates.  
479 Genotyping primers were designed to amplify a 221bp fragment of the wild type *Whamm* allele  
480 or a 222bp fragment of the knockout *Whamm* allele (Supplemental Table S1). All mice were  
481 sacrificed during the SARS-CoV-2 pandemic in 2020. Sperm is cryopreserved at JAX.

### 482 **Mouse Phenotyping**

483 Spot urine and blood were collected at 8, 16, 20, and 24 weeks-of-age. Urinary albumin,  
484 glucose, phosphate, potassium, sodium, chloride, calcium, and creatinine, and plasma glucose  
485 were measured using a Beckman Coulter DxC 700 AU chemistry analyzer. For relative  
486 quantification of amino acids in the urine, a LC-MS/MS Selected Reaction Monitoring (SRM)  
487 method was performed using a Thermo Fisher Scientific TSQ Endura equipped with a Vanquish  
488 UPLC based on Thermo Fisher's technical note 65382 adapted for smaller volumes of urine.  
489 Briefly, SRM transitions were detailed in the TraceFinder software and then verified with the  
490 Metabolomics Amino Acid Mix Standard (Cambridge Isotope Laboratories) for unique  
491 transitions. 10µL of urine was precipitated with 30% sulfosalicylic acid (final concentration 10%)

492 and vortexed for 30s. Samples were allowed to precipitate for 30min at 4°C and centrifuged to  
493 pellet protein. Supernatant was then mixed with internal standard and diluent mixture. 4μL of  
494 this final solution was injected into the platform. Chromatographic separation was performed  
495 over 18min, with an Acclaim Trinity mixed mode column. Buffer A was ammonium formate in  
496 water, pH ~3. Buffer B was acetonitrile with ammonium formate, pH ~3. Separation was  
497 achieved with a two-part separation and flow rate increase. Detection of each of the 52  
498 transitions was performed with the TSQ Endura triple quadruple mass spectrometer. Data was  
499 acquired in SRM mode using a resolution of 0.7 m/z full width at half maximum with a 500ms  
500 cycle time. Data were processed using Tracefinder 4.1 software.

### 501 **Bioinformatics**

502 Gene expression maps from adult mice were created using Kidney Cell Explorer ([Ransick et al.,](#)  
503 [2019](#)). This searchable database ([cello.shinyapps.io/kidneycellexplorer/](https://cello.shinyapps.io/kidneycellexplorer/)), consisting of single  
504 cell RNA-sequencing data clustered into distinct anatomical regions (“metacells”) of the  
505 nephron, was used to generate heat maps of the normalized average expression of genes  
506 (average expression) as well as the proportion of cells expressing a gene (expressed  
507 proportion) within each metacell.

### 508 **Kidney Histology and Immunostaining**

509 For histological analyses, kidneys were collected from 25-week-old mice in 10% neutral  
510 buffered formalin, embedded in paraffin, and subjected to periodic acid-Schiff (PAS) staining.  
511 Histological slides can be viewed at <https://images.jax.org/webclient/?show=dataset-2763>. For  
512 immunostaining, 5μm kidney sections were mounted onto charged glass slides, deparaffinized  
513 in Histo-Clear (National Diagnostics) twice, 100% ethanol twice, 95% ethanol twice, and 70%  
514 ethanol, then rehydrated in deionized water. Antigen retrieval was performed at 95°C in citrate  
515 buffer (20mM citric acid, 93mM sodium citrate in water) pH 6.0 for 30min, and slides were  
516 cooled to room temperature before 3 phosphate-buffered saline (PBS) washes. Tissue samples  
517 were incubated in blocking buffer (PBS containing 1% bovine serum albumin (BSA), 10% goat

518 serum, 0.1% Tween-20) for 2h at room temperature, washed once with PBS, probed with  
519 primary antibodies (Supplemental Table S2) for 10h at 4°C, washed 3 times, and treated with  
520 AlexaFluor-conjugated secondary antibodies and DAPI (Supplemental Table S2) for 2h at 4°C,  
521 followed by 3 PBS washes and mounting using ProLong Gold (Invitrogen) and 18mm square  
522 glass coverslips. Slides were imaged as described below.

### 523 **Kidney Tissue Preparation**

524 Kidneys were harvested from 25-week-old WHAMM<sup>WT</sup> and WHAMM<sup>KO</sup> mice after cervical  
525 dislocation and frozen at -80°C. Tissue extracts were prepared by resuspending thawed kidney  
526 thirds in tissue lysis buffer (20mM HEPES pH 7.4, 100mM NaCl, 1% IGEPAL CA-630, 1mM  
527 EDTA, 1mM Na<sub>3</sub>VO<sub>4</sub>, 1mM NaF, plus 1mM PMSF, and 10µg/ml each of aprotinin, leupeptin,  
528 pepstatin, and chymostatin) and sonicating at 60% power for 35s 3 times using a Fisher  
529 dismembranator. The lysates were then clarified by centrifugation at 21,000xg for 12min at 4°C,  
530 and the supernatants were collected and centrifuged again at 21,000xg for 6min at 4°C. Extract  
531 concentrations were measured using Bradford assays (Bio-Rad), aliquoted, and stored at -80°C.

### 532 **Cell Culture**

533 To isolate MEFs, timed matings between WHAMM<sup>HET</sup> mice were performed and embryos  
534 collected at E13.5 in Dulbecco's Modified Eagle Medium (DMEM) containing L-glutamine.  
535 Embryos were shipped on ice overnight and within 24h of harvesting, the livers, hearts, and  
536 brains were removed, and the remaining tissues were manually dissociated with scalpels.  
537 Embryonic slurries were each transferred into 3mL of 0.25% Trypsin-EDTA and incubated on  
538 ice for 18h. Without disturbing the settled tissue, 2mL of the supernatants were removed, and  
539 the remaining materials were incubated at 37°C for 30min. Each cell suspension was mixed with  
540 9mL of complete media (DMEM containing 10% fetal bovine serum (FBS), GlutaMax, and  
541 antibiotic-antimycotic (Gibco)) and allowed to adhere to a 10cm dish at 37°C in 5% CO<sub>2</sub> for 24h.  
542 Adherent cells were washed with PBS, collected in 0.05% Trypsin-EDTA, resuspended in  
543 media, and split into two new 10cm dishes. After an additional 24h of growth, the cells in one

544 dish were washed with PBS, collected in PBS containing 2mM EDTA, pelleted, resuspended in  
545 FBS containing 10% DMSO, aliquoted, and stored in liquid nitrogen. The cells in the second  
546 dish were maintained at 35-95% confluence, passaged every 2-3 days, and cryopreserved after  
547 passage 7. Upon reanimation, cells went through crisis after 3-5 more passages, and  
548 immortalized cultures eventually emerged. Experiments were conducted after passage 16.  
549 Human male HK-2 proximal tubule kidney cells (ATCC) were cultured in DMEM, 10% FBS,  
550 GlutaMax, and antibiotic-antimycotic. All experiments were performed using cells that had been  
551 in active culture for 2-10 trypsinized passages after thawing.

### 552 **Cell Genotyping**

553 MEFs grown in 6cm dishes were collected in PBS containing 1mM EDTA, centrifuged, washed  
554 with PBS, and recentrifuged. Genomic DNA was isolated from  $\sim 2 \times 10^6$  cells using the Monarch  
555 DNA purification Kit (New England Biolabs). For genotyping, PCRs were performed using 50ng  
556 of genomic DNA, gene-specific primers, and Taq polymerase (New England Biolabs). Primers  
557 (Supplemental Table S1) were designed to amplify the wild type and knockout alleles as  
558 described above, 480bp and 660bp fragments of the *Xlr* gene on the X chromosome, a 280bp  
559 fragment of the *Sly* gene on the Y chromosome, and a 241bp *Gapdh* control. PCR products  
560 were subjected to ethidium bromide agarose gel electrophoresis and visualized using ImageJ  
561 (Schindelin *et al.*, 2012). Male heterozygous ( $WHAMM^{HET}_{XY}$ ) and male homozygous *Whamm*  
562 knockout ( $WHAMM^{KO}_{XY}$ ) cell populations were generated, but we were unable to isolate male  
563 wild type MEFs despite multiple attempts.

### 564 **Immunoblotting**

565 Cells grown in 6-well plates were collected in PBS containing 1mM EDTA and centrifuged  
566 before storing at  $-20^{\circ}\text{C}$ . Pellets were resuspended in cell lysis buffer (20mM HEPES pH 7.4,  
567 50mM NaCl, 0.5mM EDTA, 1% Triton X-100, 1mM  $\text{Na}_3\text{VO}_4$ , and 1mM NaF, plus protease  
568 inhibitors). Kidney or cell extracts were diluted in SDS-PAGE sample buffer, boiled, centrifuged,  
569 and subjected to SDS-PAGE before transfer to nitrocellulose (GE Healthcare). Membranes

570 were blocked in PBS containing 5% milk (PBS-M) before being probed with primary antibodies  
571 (Supplemental Table S2) diluted in PBS-M overnight at 4°C plus an additional 2-3h at room  
572 temperature. Membranes were rinsed twice with PBS and washed thrice with PBS + 0.5%  
573 Tween-20 (PBS-T). Membranes were then probed with secondary antibodies conjugated to  
574 IRDye-800, IRDye-680, or horseradish peroxidase (Supplemental Table S2), rinsed with PBS,  
575 and washed with PBS-T. Blots were visualized using a LI-COR Odyssey Fc imaging system,  
576 band intensities determined using the Analysis tool in Image Studio software, and quantities of  
577 proteins-of-interest normalized to tubulin, actin, and/or GAPDH loading controls.

### 578 **Chemical Treatments and Transfections**

579 Cells were seeded onto 12mm glass coverslips in 24-well plates, allowed to grow for 24h, and  
580 then treated prior to fixation. MEFs were treated with media containing 50µM chloroquine  
581 (Sigma) or 10µM rapamycin (Tocris) for 16h prior to fixation. HK-2 cells were treated with media  
582 containing 50µM chloroquine, 200µM CK666 (Calbiochem), or both for 6h prior to fixation, or  
583 with media containing 5µg/mL puromycin (Sigma), or puromycin plus 200µM CK666 for 2h prior  
584 to fixation. For RNAi experiments, cells were grown in 6-well plates for 24h, transfected with  
585 40nM siRNAs (Supplemental Table S1) using RNAiMAX (Invitrogen), incubated in growth media  
586 for 24h, reseeded onto 12mm glass coverslips, and incubated for an additional 48h prior to  
587 fixation. For transgene expression, HK-2 cells grown on 12mm glass coverslips were  
588 transfected with 50-100ng of LAP-WHAMM(WT) or LAP-WHAMM(W807A) (Supplemental Table  
589 S1) using LipofectamineLTX with Plus reagent (Invitrogen) diluted in DMEM. After 5h, cells were  
590 incubated in growth media for an additional 18h prior to fixation. The LAP tag consists of an N-  
591 terminal His-EGFP-TEV-S peptide (Campellone *et al.*, 2008).

### 592 **Immunofluorescence Microscopy**

593 Cells grown on coverslips were fixed using 2.5% paraformaldehyde (PFA) in PBS for 30min,  
594 washed, permeabilized with 0.1% TritonX-100 in PBS, washed, and incubated in blocking buffer  
595 (PBS containing 1% FBS, 1% BSA, and 0.02% NaN<sub>3</sub>) for 15min. For LC3 and GABARAP



596 staining, a methanol denaturation step was included between the PFA and TritonX-100 steps.  
597 Cells were probed with primary antibodies (Supplemental Table S2) for 45min, washed, and  
598 treated with AlexaFluor-conjugated secondary antibodies, DAPI, and/or AlexaFluor-conjugated  
599 phalloidin (Supplemental Table S2) for 45min, followed by washes and mounting in ProLong  
600 Gold. All tissue and cell images were captured using a Nikon Eclipse Ti inverted microscope  
601 equipped with Plan Apo 100X/1.45, Plan Apo 60X/1.40, or Plan Fluor 20x/0.5 numerical  
602 aperture objectives, an Andor Clara-E camera, and a computer running NIS Elements software.  
603 Cells were viewed in multiple focal planes, and Z-series were captured in 0.2 $\mu$ m steps. Images  
604 presented in the figures represent either 4-5 slice projections for tissue samples or 1-3 slice  
605 projections for cell samples.

#### 606 **Image Processing and Quantification**

607 Images were processed and analyzed using ImageJ (Schindelin *et al.*, 2012). For analyses of  
608 ACE2 and Megalin fluorescence intensities per tubule, the Selection tool was used to outline  
609 proximal tubule cell clusters, the Measure tool was used to acquire their mean fluorescence  
610 intensities, and the background signals from outside of the tubules were subtracted from the  
611 mean fluorescence values. To calculate the ACE2 polarity ratios, the selection tool was used to  
612 select  $\sim 12\mu\text{m}^2$  areas in the apical and cytoplasmic regions of the cluster of proximal tubule cells,  
613 the Measure tool was used to acquire the mean fluorescence intensity in each region,  
614 background fluorescence was subtracted from these values, and the ACE2 polarity ratio was  
615 determined by dividing the apical by cytoplasmic fluorescence per tubule. To generate ACE2  
616 pixel intensity plots, an 8 $\mu$ m line was drawn through a cluster of proximal tubule cells such that  
617 the apical region was at the midpoint, and the Plot Profile tool was used to measure the intensity  
618 along the line. The background signal from outside of the tubule was subtracted from the mean  
619 fluorescence values, and the maximum ACE2 intensity for each wild type profile was set to 1.

620 For analyses of LC3/GABARAP morphology and actin localization in MEFs and HK-2s, a  
621 3-6 $\mu$ m line was drawn through a fluorescent autophagic structure, such that the center of the

622 circle or punctum was at the midpoint, and the Plot Profile tool was used to measure the  
623 intensity along the line. To determine the fluorescence intensities of LC3 and GABARAP, the  
624 Selection tool was used to outline individual cells, and the Measure tool was used to acquire  
625 total fluorescence. The number of GABARAP puncta per cell was counted manually. To  
626 calculate the puncta-to-cytoplasmic ratio of GABARAP fluorescence, the Selection tool was  
627 used to select GABARAP puncta or an equivalently-sized area of the cytoplasm, the Measure  
628 tool was used to acquire the mean fluorescence intensity in each area, and the puncta-to-  
629 cytoplasmic GABARAP fluorescence ratio was determined. The percentage of cells with LC3-  
630 positive rings and the number of LC3-positive rings per cell were counted manually. The  
631 percentage of cells with STX17-positive vesicles and the number of STX17-positive vesicles per  
632 cell were counted manually. Vesicles were confirmed to be autophagic based on LC3 staining.

### 633 **Reproducibility and Statistics**

634 For urinalyses, quantifications were based on data from 4-10 mice of a given genotype. For  
635 kidney tissue immunoblotting and immunostaining, quantifications were based on data from  
636 kidneys from 3-5 mice per genotype. For cell-based assays, conclusions were based on  
637 observations made from at least 3 separate experiments, and quantifications were based on  
638 data from 3 representative experiments. The sample size used for statistical tests was the  
639 number of mice or the number of times an experiment was performed. Statistical analyses were  
640 performed using GraphPad Prism software. Statistics for data sets comparing 2 conditions were  
641 determined using unpaired t-tests as noted in the Legends. Statistics for data sets with 3 or  
642 more conditions were performed using ANOVAs followed by Tukey's post-hoc test unless  
643 otherwise indicated. P-values <0.05 were considered statistically significant.

644 **ACKNOWLEDGEMENTS**

645 We gratefully acknowledge the contribution of Dorothy Ahlf Wheatcraft and the Protein Sciences  
646 and Histopathology Sciences services at The Jackson Laboratory for expert assistance with the  
647 work described in this publication. We also thank Naydu Nunno for help processing kidney  
648 samples and Campellone Lab members for their comments on this manuscript. KGC was  
649 supported by National Institutes of Health grants GM107441 and AG050774 ([www.nih.gov](http://www.nih.gov)). RK  
650 was supported by National Institutes of Health grants ES29916, AG038070, DK131019, and  
651 DK131061, and the Alport Syndrome Foundation. The funders had no role in study design, data  
652 collection and analysis, decision to publish, or preparation of the manuscript.

## 653 REFERENCES

- 654 Alekhina, O., Burstein, E., and Billadeau, D.D. (2017). Cellular functions of WASP family  
655 proteins at a glance. *J Cell Sci* 130, 2235-2241.
- 656 Arrondel, C., Missouri, S., Snoek, R., Patat, J., Menara, G., Collinet, B., Liger, D., Durand, D.,  
657 Gribouval, O., Boyer, O., et al. (2019). Defects in t(6)A tRNA modification due to GON7 and  
658 YRDC mutations lead to Galloway-Mowat syndrome. *Nat Commun* 10, 3967.
- 659 Axe, E.L., Walker, S.A., Manifava, M., Chandra, P., Roderick, H.L., Habermann, A., Griffiths, G.,  
660 and Ktistakis, N.T. (2008). Autophagosome formation from membrane compartments enriched  
661 in phosphatidylinositol 3-phosphate and dynamically connected to the endoplasmic reticulum. *J*  
662 *Cell Biol* 182, 685-701.
- 663 Ballabio, A., and Bonifacino, J.S. (2020). Lysosomes as dynamic regulators of cell and  
664 organismal homeostasis. *Nat Rev Mol Cell Biol* 21, 101-118.
- 665 Ben-Omran, T., Fahiminiya, S., Sorfazlian, N., Almurieki, M., Nawaz, Z., Nadaf, J., Khadija,  
666 K.A., Zaineddin, S., Kamel, H., Majewski, J., et al. (2015). Nonsense mutation in the WDR73  
667 gene is associated with Galloway-Mowat syndrome. *J Med Genet* 52, 381-390.
- 668 Berquez, M., Gadsby, J.R., Festa, B.P., Butler, R., Jackson, S.P., Berno, V., Luciani, A.,  
669 Devuyst, O., and Gallop, J.L. (2020). The phosphoinositide 3-kinase inhibitor alpelisib restores  
670 actin organization and improves proximal tubule dysfunction in vitro and in a mouse model of  
671 Lowe syndrome and Dent disease. *Kidney Int* 98, 883-896.
- 672 Bockenbauer, D., Bokenkamp, A., van't Hoff, W., Levtchenko, E., Kist-van Holthe, J.E., Tasic,  
673 V., and Ludwig, M. (2008). Renal phenotype in Lowe Syndrome: a selective proximal tubular  
674 dysfunction. *Clin J Am Soc Nephrol* 3, 1430-1436.
- 675 Braun, D.A., Rao, J., Mollet, G., Schapiro, D., Daugeron, M.C., Tan, W., Gribouval, O., Boyer,  
676 O., Revy, P., Jobst-Schwan, T., et al. (2017). Mutations in KEOPS-complex genes cause  
677 nephrotic syndrome with primary microcephaly. *Nat Genet* 49, 1529-1538.
- 678 Braun, D.A., Shril, S., Sinha, A., Schneider, R., Tan, W., Ashraf, S., Hermle, T., Jobst-Schwan,  
679 T., Widmeier, E., Majmundar, A.J., et al. (2018). Mutations in WDR4 as a new cause of  
680 Galloway-Mowat syndrome. *Am J Med Genet A* 176, 2460-2465.
- 681 Campellone, K.G., Lebek, N.M., and King, V.L. (2023). Branching out in different directions:  
682 Emerging cellular functions for the Arp2/3 complex and WASP-family actin nucleation factors.  
683 *Eur J Cell Biol* 102, 151301.
- 684 Campellone, K.G., Webb, N.J., Znameroski, E.A., and Welch, M.D. (2008). WHAMM is an  
685 Arp2/3 complex activator that binds microtubules and functions in ER to Golgi transport. *Cell*  
686 134, 148-161.
- 687 Campellone, K.G., and Welch, M.D. (2010). A nucleator arms race: cellular control of actin  
688 assembly. *Nat Rev Mol Cell Biol* 11, 237-251.
- 689 Colin, E., Huynh Cong, E., Mollet, G., Guichet, A., Gribouval, O., Arrondel, C., Boyer, O., Daniel,  
690 L., Gubler, M.C., Ekin, Z., et al. (2014). Loss-of-function mutations in WDR73 are responsible  
691 for microcephaly and steroid-resistant nephrotic syndrome: Galloway-Mowat syndrome. *Am J*  
692 *Hum Genet* 95, 637-648.
- 693 Courtland, J.L., Bradshaw, T.W., Waitt, G., Soderblom, E.J., Ho, T., Rajab, A., Vancini, R., Kim,  
694 I.H., and Soderling, S.H. (2021). Genetic disruption of WASHC4 drives endo-lysosomal  
695 dysfunction and cognitive-movement impairments in mice and humans. *Elife* 10.
- 696 Coutts, A.S., and La Thangue, N.B. (2015). Actin nucleation by WH2 domains at the  
697 autophagosome. *Nat Commun* 6, 7888.
- 698 Cybulsky, A.V. (2017). Endoplasmic reticulum stress, the unfolded protein response and  
699 autophagy in kidney diseases. *Nat Rev Nephrol* 13, 681-696.
- 700 Dai, A., Yu, L., and Wang, H.W. (2019). WHAMM initiates autolysosome tubulation by  
701 promoting actin polymerization on autolysosomes. *Nat Commun* 10, 3699.

702 Daste, F., Walrant, A., Holst, M.R., Gadsby, J.R., Mason, J., Lee, J.E., Brook, D., Mettlen, M.,  
703 Larsson, E., Lee, S.F., et al. (2017). Control of actin polymerization via the coincidence of  
704 phosphoinositides and high membrane curvature. *J Cell Biol* 216, 3745-3765.

705 De Leo, M.G., Staiano, L., Vicinanza, M., Luciani, A., Carissimo, A., Mutarelli, M., Di Campi, A.,  
706 Polishchuk, E., Di Tullio, G., Morra, V., et al. (2016). Autophagosome-lysosome fusion triggers a  
707 lysosomal response mediated by TLR9 and controlled by OCRL. *Nat Cell Biol* 18, 839-850.

708 De Matteis, M.A., Staiano, L., Emma, F., and Devuyst, O. (2017). The 5-phosphatase OCRL in  
709 Lowe syndrome and Dent disease 2. *Nat Rev Nephrol* 13, 455-470.

710 Derry, J.M., Ochs, H.D., and Francke, U. (1994). Isolation of a novel gene mutated in Wiskott-  
711 Aldrich syndrome. *Cell* 78, 635-644.

712 Devereaux, K., Dall'Armi, C., Alcazar-Roman, A., Ogasawara, Y., Zhou, X., Wang, F.,  
713 Yamamoto, A., De Camilli, P., and Di Paolo, G. (2013). Regulation of mammalian autophagy by  
714 class II and III PI 3-kinases through PI3P synthesis. *PLoS One* 8, e76405.

715 Dikic, I., and Elazar, Z. (2018). Mechanism and medical implications of mammalian autophagy.  
716 *Nat Rev Mol Cell Biol* 19, 349-364.

717 El Younsi, M., Kraoua, L., Meddeb, R., Ferjani, M., Trabelsi, M., Ouertani, I., Maazoul, F., Abid,  
718 N., Gargah, T., and M'Rad, R. (2019). WDR73-related galloway mowat syndrome with  
719 collapsing glomerulopathy. *Eur J Med Genet* 62, 103550.

720 Festa, B.P., Berquez, M., Gassama, A., Amrein, I., Ismail, H.M., Samardzija, M., Staiano, L.,  
721 Luciani, A., Grimm, C., Nussbaum, R.L., et al. (2019). OCRL deficiency impairs endolysosomal  
722 function in a humanized mouse model for Lowe syndrome and Dent disease. *Hum Mol Genet*  
723 28, 1931-1946.

724 Gautreau, A.M., Fregoso, F.E., Simanov, G., and Dominguez, R. (2021). Nucleation,  
725 stabilization, and disassembly of branched actin networks. *Trends Cell Biol*.

726 Gomez, T.S., Gorman, J.A., de Narvajias, A.A., Koenig, A.O., and Billadeau, D.D. (2012).  
727 Trafficking defects in WASH-knockout fibroblasts originate from collapsed endosomal and  
728 lysosomal networks. *Mol Biol Cell* 23, 3215-3228.

729 Grieco, G., Janssens, V., Gaide Chevronnay, H.P., N'Kuli, F., Van Der Smissen, P., Wang, T.,  
730 Shan, J., Vainio, S., Bilanges, B., Jouret, F., et al. (2018). Vps34/PI3KC3 deletion in kidney  
731 proximal tubules impairs apical trafficking and blocks autophagic flux, causing a Fanconi-like  
732 syndrome and renal insufficiency. *Sci Rep* 8, 14133.

733 Harris, A.N., Lee, H.W., Osis, G., Fang, L., Webster, K.L., Verlander, J.W., and Weiner, I.D.  
734 (2018). Differences in renal ammonia metabolism in male and female kidney. *Am J Physiol*  
735 *Renal Physiol* 315, F211-F222.

736 Hoopes, R.R., Jr., Shrimpton, A.E., Knohl, S.J., Hueber, P., Hoppe, B., Matyus, J., Simckes, A.,  
737 Tasic, V., Toenshoff, B., Suchy, S.F., et al. (2005). Dent Disease with mutations in OCRL1. *Am*  
738 *J Hum Genet* 76, 260-267.

739 Hu, R., McDonough, A.A., and Layton, A.T. (2020). Sex differences in solute transport along the  
740 nephrons: effects of Na(+) transport inhibition. *Am J Physiol Renal Physiol* 319, F487-F505.

741 Hu, X., and Mullins, R.D. (2019). LC3 and STRAP regulate actin filament assembly by JMY  
742 during autophagosome formation. *J Cell Biol* 218, 251-266.

743 Inoue, K., Balkin, D.M., Liu, L., Nandez, R., Wu, Y., Tian, X., Wang, T., Nussbaum, R., De  
744 Camilli, P., and Ishibe, S. (2017). Kidney Tubular Ablation of Ocr1/Inpp5b Phenocopies Lowe  
745 Syndrome Tubulopathy. *J Am Soc Nephrol* 28, 1399-1407.

746 Itakura, E., Kishi-Itakura, C., and Mizushima, N. (2012). The hairpin-type tail-anchored SNARE  
747 syntaxin 17 targets to autophagosomes for fusion with endosomes/lysosomes. *Cell* 151, 1256-  
748 1269.

749 Ito, Y., Carss, K.J., Duarte, S.T., Hartley, T., Keren, B., Kurian, M.A., Marey, I., Charles, P.,  
750 Mendonca, C., Nava, C., et al. (2018). De Novo Truncating Mutations in WASF1 Cause  
751 Intellectual Disability with Seizures. *Am J Hum Genet* 103, 144-153.

752 Jiang, C., Gai, N., Zou, Y., Zheng, Y., Ma, R., Wei, X., Liang, D., and Wu, L. (2017). WDR73  
753 missense mutation causes infantile onset intellectual disability and cerebellar hypoplasia in a  
754 consanguineous family. *Clin Chim Acta* 464, 24-29.

755 Jinks, R.N., Puffenberger, E.G., Baple, E., Harding, B., Crino, P., Fogo, A.B., Wenger, O., Xin,  
756 B., Koehler, A.E., McGlincy, M.H., et al. (2015). Recessive nephrocerebellar syndrome on the  
757 Galloway-Mowat syndrome spectrum is caused by homozygous protein-truncating mutations of  
758 WDR73. *Brain* 138, 2173-2190.

759 Johansen, T., and Lamark, T. (2020). Selective Autophagy: ATG8 Family Proteins, LIR Motifs  
760 and Cargo Receptors. *J Mol Biol* 432, 80-103.

761 Kabrawala, S., Zimmer, M.D., and Campellone, K.G. (2020). WHIMP links the actin nucleation  
762 machinery to Src-family kinase signaling during protrusion and motility. *PLoS Genet* 16,  
763 e1008694.

764 Kast, D.J., Zajac, A.L., Holzbaaur, E.L., Ostap, E.M., and Dominguez, R. (2015). WHAMM  
765 Directs the Arp2/3 Complex to the ER for Autophagosome Biogenesis through an Actin Comet  
766 Tail Mechanism. *Curr Biol* 25, 1791-1797.

767 Kerjaschki, D., Noronha-Blob, L., Sacktor, B., and Farquhar, M.G. (1984). Microdomains of  
768 distinctive glycoprotein composition in the kidney proximal tubule brush border. *J Cell Biol* 98,  
769 1505-1513.

770 King, V.L., and Campellone, K.G. (2023). F-actin-rich territories coordinate apoptosome  
771 assembly and caspase activation during DNA-damage induced intrinsic apoptosis. *Mol Biol Cell*  
772 34, ar41.

773 King, V.L., Leclair, N.K., Coulter, A.M., and Campellone, K.G. (2021). The actin nucleation  
774 factors JMY and WHAMM enable a rapid Arp2/3 complex-mediated intrinsic pathway of  
775 apoptosis. *PLoS Genet* 17, e1009512.

776 Klionsky, D.J., Abdel-Aziz, A.K., Abdelfatah, S., Abdellatif, M., Abdoli, A., Abel, S., Abeliovich,  
777 H., Abildgaard, M.H., Abudu, Y.P., Acevedo-Arozena, A., et al. (2021). Guidelines for the use  
778 and interpretation of assays for monitoring autophagy (4th edition)(1). *Autophagy* 17, 1-382.

779 Klootwijk, E.D., Reichold, M., Unwin, R.J., Kleta, R., Warth, R., and Bockenhauer, D. (2015).  
780 Renal Fanconi syndrome: taking a proximal look at the nephron. *Nephrol Dial Transplant* 30,  
781 1456-1460.

782 Kounakis, K., and Tavernarakis, N. (2019). The Cytoskeleton as a Modulator of Aging and  
783 Neurodegeneration. *Adv Exp Med Biol* 1178, 227-245.

784 Kramer, D.A., Piper, H.K., and Chen, B. (2022). WASP family proteins: Molecular mechanisms  
785 and implications in human disease. *Eur J Cell Biol* 101, 151244.

786 Lazarou, M., Sliter, D.A., Kane, L.A., Sarraf, S.A., Wang, C., Burman, J.L., Sideris, D.P., Fogel,  
787 A.I., and Youle, R.J. (2015). The ubiquitin kinase PINK1 recruits autophagy receptors to induce  
788 mitophagy. *Nature* 524, 309-314.

789 Lemaire, M. (2021). Novel Fanconi renotubular syndromes provide insights in proximal tubule  
790 pathophysiology. *Am J Physiol Renal Physiol* 320, F145-F160.

791 Levine, B., and Kroemer, G. (2019). Biological Functions of Autophagy Genes: A Disease  
792 Perspective. *Cell* 176, 11-42.

793 Li, H., Liu, F., Kuang, H., Teng, H., Chen, S., Zeng, S., Zhou, Q., Li, Z., Liang, D., Li, Z., et al.  
794 (2022). WDR73 Depletion Destabilizes PIP4K2C Activity and Impairs Focal Adhesion Formation  
795 in Galloway-Mowat Syndrome. *Biology (Basel)* 11.

796 Li, Q., McDonough, A.A., Layton, H.E., and Layton, A.T. (2018). Functional implications of  
797 sexual dimorphism of transporter patterns along the rat proximal tubule: modeling and analysis.  
798 *Am J Physiol Renal Physiol* 315, F692-F700.

799 Mann, N., Mzoughi, S., Schneider, R., Kuhl, S.J., Schanze, D., Klambt, V., Lovric, S., Mao, Y.,  
800 Shi, S., Tan, W., et al. (2021). Mutations in PRDM15 Are a Novel Cause of Galloway-Mowat  
801 Syndrome. *J Am Soc Nephrol* 32, 580-596.

802 Mathiowetz, A.J., Baple, E., Russo, A.J., Coulter, A.M., Carrano, E., Brown, J.D., Jinks, R.N.,  
803 Crosby, A.H., and Campellone, K.G. (2017). An Amish founder mutation disrupts a PI(3)P-  
804 WHAMM-Arp2/3 complex-driven autophagosomal remodeling pathway. *Mol Biol Cell* 28, 2492-  
805 2507.

806 Mehta, Z.B., Pietka, G., and Lowe, M. (2014). The cellular and physiological functions of the  
807 Lowe syndrome protein OCRL1. *Traffic* 15, 471-487.

808 Mi, N., Chen, Y., Wang, S., Chen, M., Zhao, M., Yang, G., Ma, M., Su, Q., Luo, S., Shi, J., et al.  
809 (2015). CapZ regulates autophagosomal membrane shaping by promoting actin assembly  
810 inside the isolation membrane. *Nat Cell Biol* 17, 1112-1123.

811 Mizushima, N. (2020). The ATG conjugation systems in autophagy. *Curr Opin Cell Biol* 63, 1-10.

812 Molinie, N., and Gautreau, A. (2018). The Arp2/3 Regulatory System and Its Deregulation in  
813 Cancer. *Physiol Rev* 98, 215-238.

814 Nakamura, S., and Yoshimori, T. (2017). New insights into autophagosome-lysosome fusion. *J*  
815 *Cell Sci* 130, 1209-1216.

816 Nguyen, T.N., Padman, B.S., Usher, J., Oorschot, V., Ramm, G., and Lazarou, M. (2016). Atg8  
817 family LC3/GABARAP proteins are crucial for autophagosome-lysosome fusion but not  
818 autophagosome formation during PINK1/Parkin mitophagy and starvation. *J Cell Biol* 215, 857-  
819 874.

820 Norden, A.G.W., Lapsley, M., Igarashi, T., Kelleher, C.L., Lee, P.J., Matsuyama, T., Scheinman,  
821 S.J., Shiraga, H., Sundin, D.P., Thakker, R.V., et al. (2002). Urinary megalin deficiency  
822 implicates abnormal tubular endocytic function in Fanconi syndrome. *J Am Soc Nephrol* 13,  
823 125-133.

824 Oltrabella, F., Pietka, G., Ramirez, I.B., Mironov, A., Starborg, T., Drummond, I.A., Hinchliffe,  
825 K.A., and Lowe, M. (2015). The Lowe syndrome protein OCRL1 is required for endocytosis in  
826 the zebrafish pronephric tubule. *PLoS Genet* 11, e1005058.

827 Pankiv, S., Clausen, T.H., Lamark, T., Brech, A., Bruun, J.A., Outzen, H., Overvatn, A., Bjorkoy,  
828 G., and Johansen, T. (2007). p62/SQSTM1 binds directly to Atg8/LC3 to facilitate degradation of  
829 ubiquitinated protein aggregates by autophagy. *J Biol Chem* 282, 24131-24145.

830 Pollard, T.D. (2016). Actin and Actin-Binding Proteins. *Cold Spring Harb Perspect Biol* 8.

831 Ransick, A., Lindstrom, N.O., Liu, J., Zhu, Q., Guo, J.J., Alvarado, G.F., Kim, A.D., Black, H.G.,  
832 Kim, J., and McMahon, A.P. (2019). Single-Cell Profiling Reveals Sex, Lineage, and Regional  
833 Diversity in the Mouse Kidney. *Dev Cell* 51, 399-413 e397.

834 Rinschen, M.M., Harder, J.L., Carter-Timofte, M.E., Zanon Rodriguez, L., Mirabelli, C., Demir,  
835 F., Kurmasheva, N., Ramakrishnan, S.K., Kunke, M., Tan, Y., et al. (2022). VPS34-dependent  
836 control of apical membrane function of proximal tubule cells and nutrient recovery by the kidney.  
837 *Sci Signal* 15, eabo7940.

838 Rivers, E., and Thrasher, A.J. (2017). Wiskott-Aldrich syndrome protein: Emerging mechanisms  
839 in immunity. *Eur J Immunol* 47, 1857-1866.

840 Ropers, F., Derivery, E., Hu, H., Garshasbi, M., Karbasiyan, M., Herold, M., Nurnberg, G.,  
841 Ullmann, R., Gautreau, A., Sperling, K., et al. (2011). Identification of a novel candidate gene for  
842 non-syndromic autosomal recessive intellectual disability: the WASH complex member SWIP.  
843 *Hum Mol Genet* 20, 2585-2590.

844 Rosti, R.O., Sotak, B.N., Bielas, S.L., Bhat, G., Silhavy, J.L., Aslanger, A.D., Altunoglu, U.,  
845 Bilge, I., Tasdemir, M., Yzaguirrem, A.D., et al. (2017). Homozygous mutation in NUP107 leads  
846 to microcephaly with steroid-resistant nephrotic condition similar to Galloway-Mowat syndrome.  
847 *J Med Genet* 54, 399-403.

848 Rottner, K., Faix, J., Bogdan, S., Linder, S., and Kerkhoff, E. (2017). Actin assembly  
849 mechanisms at a glance. *J Cell Sci* 130, 3427-3435.

850 Russo, A.J., Mathiowetz, A.J., Hong, S., Welch, M.D., and Campellone, K.G. (2016). Rab1  
851 recruits WHAMM during membrane remodeling but limits actin nucleation. *Mol Biol Cell* 27, 967-  
852 978.

853 Sarraf, S.A., Shah, H.V., Kanfer, G., Pickrell, A.M., Holtzclaw, L.A., Ward, M.E., and Youle, R.J.  
854 (2020). Loss of TAX1BP1-Directed Autophagy Results in Protein Aggregate Accumulation in the  
855 Brain. *Mol Cell* 80, 779-795 e710.

856 Schell, C., Baumhagl, L., Salou, S., Conzelmann, A.C., Meyer, C., Helmstadter, M., Wrede, C.,  
857 Grahammer, F., Eimer, S., Kerjaschki, D., et al. (2013). N-wasp is required for stabilization of  
858 podocyte foot processes. *J Am Soc Nephrol* 24, 713-721.

859 Schell, C., Sabass, B., Helmstaedter, M., Geist, F., Abed, A., Yasuda-Yamahara, M., Sigle, A.,  
860 Maier, J.I., Grahammer, F., Siegerist, F., et al. (2018). ARP3 Controls the Podocyte Architecture  
861 at the Kidney Filtration Barrier. *Dev Cell* 47, 741-757 e748.

862 Schindelin, J., Arganda-Carreras, I., Frise, E., Kaynig, V., Longair, M., Pietzsch, T., Preibisch,  
863 S., Rueden, C., Saalfeld, S., Schmid, B., et al. (2012). Fiji: an open-source platform for  
864 biological-image analysis. *Nat Methods* 9, 676-682.

865 Schluter, K., Waschbusch, D., Anft, M., Hugging, D., Kind, S., Hanisch, J., Lakisic, G.,  
866 Gautreau, A., Barnekow, A., and Stradal, T.E. (2014). JMY is involved in anterograde vesicle  
867 trafficking from the trans-Golgi network. *Eur J Cell Biol* 93, 194-204.

868 Shang, D., Wang, L., Klionsky, D.J., Cheng, H., and Zhou, R. (2021). Sex differences in  
869 autophagy-mediated diseases: toward precision medicine. *Autophagy* 17, 1065-1076.

870 Shen, Q.T., Hsiue, P.P., Sindelar, C.V., Welch, M.D., Campellone, K.G., and Wang, H.W.  
871 (2012). Structural insights into WHAMM-mediated cytoskeletal coordination during membrane  
872 remodeling. *J Cell Biol* 199, 111-124.

873 Shikama, N., Lee, C.W., France, S., Delavaine, L., Lyon, J., Krstic-Demonacos, M., and La  
874 Thangue, N.B. (1999). A novel cofactor for p300 that regulates the p53 response. *Mol Cell* 4,  
875 365-376.

876 Snapper, S.B., Takeshima, F., Anton, I., Liu, C.H., Thomas, S.M., Nguyen, D., Dudley, D.,  
877 Fraser, H., Purich, D., Lopez-Illasaca, M., et al. (2001). N-WASP deficiency reveals distinct  
878 pathways for cell surface projections and microbial actin-based motility. *Nat Cell Biol* 3, 897-  
879 904.

880 Srivastava, S., Macke, E.L., Swanson, L.C., Coulter, D., Klee, E.W., Mullegama, S.V., Xie, Y.,  
881 Lanpher, B.C., Bedoukian, E.C., Skraban, C.M., et al. (2021). Expansion of the Genotypic and  
882 Phenotypic Spectrum of WASF1-Related Neurodevelopmental Disorder. *Brain Sci* 11.

883 Suchy, S.F., and Nussbaum, R.L. (2002). The deficiency of PIP2 5-phosphatase in Lowe  
884 syndrome affects actin polymerization. *Am J Hum Genet* 71, 1420-1427.

885 Tang, C., Livingston, M.J., Liu, Z., and Dong, Z. (2020). Autophagy in kidney homeostasis and  
886 disease. *Nat Rev Nephrol* 16, 489-508.

887 Tilley, F.C., Arrondel, C., Chhuon, C., Boisson, M., Cagnard, N., Parisot, M., Menara, G., Lefort,  
888 N., Guerrero, I.C., Bole-Feysot, C., et al. (2021). Disruption of pathways regulated by Integrator  
889 complex in Galloway-Mowat syndrome due to WDR73 mutations. *Sci Rep* 11, 5388.

890 Torres-Pinzon, D.L., Ralph, D.L., Veiras, L.C., and McDonough, A.A. (2021). Sex-specific  
891 adaptations to high-salt diet preserve electrolyte homeostasis with distinct sodium transporter  
892 profiles. *Am J Physiol Cell Physiol* 321, C897-C909.

893 Tsuboyama, K., Koyama-Honda, I., Sakamaki, Y., Koike, M., Morishita, H., and Mizushima, N.  
894 (2016). The ATG conjugation systems are important for degradation of the inner  
895 autophagosomal membrane. *Science* 354, 1036-1041.

896 Utsch, B., Bokenkamp, A., Benz, M.R., Besbas, N., Dotsch, J., Franke, I., Frund, S., Gok, F.,  
897 Hoppe, B., Karle, S., et al. (2006). Novel OCRL1 mutations in patients with the phenotype of  
898 Dent disease. *Am J Kidney Dis* 48, 942 e941-914.

899 Valdmánis, P.N., Meijer, I.A., Reynolds, A., Lei, A., MacLeod, P., Schlesinger, D., Zatz, M.,  
900 Reid, E., Dion, P.A., Drapeau, P., et al. (2007). Mutations in the KIAA0196 gene at the SPG8  
901 locus cause hereditary spastic paraplegia. *Am J Hum Genet* 80, 152-161.

902 van der Wijst, J., Belge, H., Bindels, R.J.M., and Devuyst, O. (2019). Learning Physiology From  
903 Inherited Kidney Disorders. *Physiol Rev* 99, 1575-1653.



904 Vargas, J.N.S., Hamasaki, M., Kawabata, T., Youle, R.J., and Yoshimori, T. (2023). The  
905 mechanisms and roles of selective autophagy in mammals. *Nat Rev Mol Cell Biol* 24, 167-185.  
906 Veiras, L.C., Girardi, A.C.C., Curry, J., Pei, L., Ralph, D.L., Tran, A., Castelo-Branco, R.C.,  
907 Pastor-Soler, N., Arranz, C.T., Yu, A.S.L., et al. (2017). Sexual Dimorphic Pattern of Renal  
908 Transporters and Electrolyte Homeostasis. *J Am Soc Nephrol* 28, 3504-3517.  
909 Vicinanza, M., Di Campli, A., Polishchuk, E., Santoro, M., Di Tullio, G., Godi, A., Levtchenko, E.,  
910 De Leo, M.G., Polishchuk, R., Sandoval, L., et al. (2011). OCRL controls trafficking through  
911 early endosomes via PtdIns4,5P(2)-dependent regulation of endosomal actin. *EMBO J* 30,  
912 4970-4985.  
913 Vodopituz, J., Seidl, R., Prayer, D., Khan, M.I., Mayr, J.A., Streubel, B., Steiss, J.O., Hahn, A.,  
914 Csaicsich, D., Castro, C., et al. (2015). WDR73 Mutations Cause Infantile Neurodegeneration  
915 and Variable Glomerular Kidney Disease. *Hum Mutat* 36, 1021-1028.  
916 Warner, F.J., Lew, R.A., Smith, A.I., Lambert, D.W., Hooper, N.M., and Turner, A.J. (2005).  
917 Angiotensin-converting enzyme 2 (ACE2), but not ACE, is preferentially localized to the apical  
918 surface of polarized kidney cells. *J Biol Chem* 280, 39353-39362.  
919 Wu, K., Seylani, A., Wu, J., Wu, X., Bleck, C.K.E., and Sack, M.N. (2021).  
920 BLOC1S1/GCN5L1/BORCS1 is a critical mediator for the initiation of autolysosomal tubulation.  
921 *Autophagy* 17, 1-18.  
922 Xia, P., Wang, S., Du, Y., Zhao, Z., Shi, L., Sun, L., Huang, G., Ye, B., Li, C., Dai, Z., et al.  
923 (2013). WASH inhibits autophagy through suppression of Beclin 1 ubiquitination. *EMBO J* 32,  
924 2685-2696.  
925 Yan, C., Martinez-Quiles, N., Eden, S., Shibata, T., Takeshima, F., Shinkura, R., Fujiwara, Y.,  
926 Bronson, R., Snapper, S.B., Kirschner, M.W., et al. (2003). WAVE2 deficiency reveals distinct  
927 roles in embryogenesis and Rac-mediated actin-based motility. *EMBO J* 22, 3602-3612.  
928 Zhang, X., Jefferson, A.B., Auethavekiat, V., and Majerus, P.W. (1995). The protein deficient in  
929 Lowe syndrome is a phosphatidylinositol-4,5-bisphosphate 5-phosphatase. *Proc Natl Acad Sci*  
930 *U S A* 92, 4853-4856.  
931 Zhao, Y.G., and Zhang, H. (2019). Autophagosome maturation: An epic journey from the ER to  
932 lysosomes. *J Cell Biol* 218, 757-770.  
933 Zuchero, J.B., Coutts, A.S., Quinlan, M.E., Thangue, N.B., and Mullins, R.D. (2009). p53-  
934 cofactor JMY is a multifunctional actin nucleation factor. *Nat Cell Biol* 11, 451-459.

935

936 **FIGURE LEGENDS**

937 **Figure 1. Male WHAMM<sup>KO</sup> mice excrete elevated levels of albumin, glucose, phosphate,**  
938 **and potassium in their urine. (A)** The mouse *Whamm* gene is 25kb in length and contains 10  
939 exons. A floxed allele containing IRES-*lacZ* and neo cassettes between exons 2 and 3, as well  
940 as *loxP* sites between the cassettes and flanking exon 3 was generated. Following Cre-  
941 mediated recombination, a knockout allele was created. Internal ribosome entry site (IRES);  
942 splice acceptor (SA); polyadenylation (pA); flippase recombination target (FRT). **(B)** Urine  
943 samples were collected from male and female wild type (WT; filled circles) or WHAMM knockout  
944 (KO; open circles) mice at 24 weeks-of-age and subjected to urinalysis. Urinary albumin-to-  
945 creatinine (ACR) ratios are plotted. Each circle represents one mouse. Statistical bars display  
946 the mean  $\pm$ SD from n=7-10 mice. **(C)** Urinary glucose-to-creatinine (GCR) ratios for males from  
947 8 to 24 weeks-of-age are plotted. Each circle represents the mean  $\pm$ SE from n=6-9 mice per  
948 genotype for each timepoint. **(D)** Plasma glucose-to-creatinine ratios for males at 24 weeks-of-  
949 age are plotted. Statistical bars display the mean  $\pm$ SD from n=8 mice. **(E)** Urinary phosphate  
950 (PhosCR), potassium (KCR), sodium (NaCR), chloride (ClCR), and calcium (CaCR) to  
951 creatinine ratios are plotted. Each circle represents one male mouse at 24 weeks. Statistical  
952 bars display the mean  $\pm$ SD from n=4-8 mice. Significant p-values are noted (unpaired t-tests).  
953

954 **Figure 2. Male WHAMM<sup>KO</sup> mice excrete elevated levels of amino acids in their urine.**  
955 Urine samples were collected from male wild type (WT; black bars) or WHAMM knockout (KO;  
956 white bars) mice at 24 weeks-of-age, and urinary amino acids were measured using mass  
957 spectrometry. AU = arbitrary units. Each bar represents the mean  $\pm$ SD from n=5-6 mice.  
958 Significant p-values are noted (ANOVA).

959

960 **Figure 3. Polarized ACE2 staining in the kidney proximal tubule is reduced in male**  
961 **WHAMM<sup>KO</sup> mice. (A)** Kidney tissue sections from wild type (WHAMM<sup>WT</sup>) or WHAMM knockout

962 (WHAMM<sup>KO</sup>) male mice were stained with ACE2 antibodies (green) and DAPI (DNA; blue).  
963 Scale bar, 50µm. **(B)** The ACE2 fluorescence intensity per tubule was calculated in ImageJ.  
964 Each circle represents the average ACE2 kidney staining from an individual mouse in which  
965 approximately 75 tubules were examined. Statistical bars represent the mean ±SD from n=5  
966 mice. **(C)** The ACE2 polarity ratio was calculated in ImageJ by dividing the fluorescence  
967 intensity in an apical region of the tubule by the intensity in a cytoplasmic region. Each circle  
968 represents the average ratio from an individual mouse in which 40 tubules were examined.  
969 Statistical bars represent the mean ±SD from n=4 mice. **(D)** Kidney tissue sections from (A)  
970 were used to generate pixel intensity profiles. Lines were drawn through the center of the  
971 tubule, and the ACE2 intensity along the line was plotted. The origin of each line is indicated  
972 with a 0. Plotted points represent the normalized mean ACE2 fluorescence ±SD from n=3 mice  
973 per genotype (comprising 3 pixel intensity plots per mouse). RFU = relative fluorescence units.  
974 Significant p-values are noted (unpaired t-tests).

975

976 **Figure 4. The lipidated form of the autophagosomal protein LC3 is more abundant in**  
977 **male WHAMM<sup>KO</sup> kidneys. (A)** Kidneys were harvested from 5 male WHAMM<sup>WT</sup> and 5 male  
978 WHAMM<sup>KO</sup> mice. 50µg extract samples were subjected to SDS-PAGE and immunoblotted with  
979 antibodies to LC3, GABARAP, tubulin, actin, and GAPDH. **(B)** LC3 and GABARAP band  
980 intensities in (A) were quantified relative to tubulin, actin, and GAPDH, and the mean  
981 normalized values were plotted. The LC3-II:I ratio was calculated by dividing the LC3-II band  
982 intensity by the LC3-I band intensity within each non-normalized sample. Statistical bars  
983 represent the mean ±SD from n=5 mice. Significant p-values are noted (unpaired t-tests).

984

985 **Figure 5. Autophagosome organization and actin recruitment are altered in WHAMM-**  
986 **deficient fibroblasts. (A-B)** Male heterozygous (WHAMM<sup>HET</sup>) and WHAMM knockout  
987 (WHAMM<sup>KO</sup>) mouse embryonic fibroblasts (MEFs) were treated with chloroquine for 16h before

988 being fixed and stained with LC3 antibodies (green), an actin antibody (magenta), and DAPI  
989 (DNA; blue). Scale bar, 25 $\mu$ m. Magnifications highlight areas of actin recruitment to LC3- or  
990 GABARAP-positive structures in WHAMM<sup>HET</sup> cells (i) and a lack of actin enrichment at  
991 autophagosomal puncta in WHAMM<sup>KO</sup> cells (ii). Lines were drawn through the images to  
992 measure pixel intensity profiles. The origin of each line is indicated with a 0. **(C)** Mean LC3 and  
993 GABARAP fluorescence values per cell were measured in ImageJ. Each bar represents the  
994 mean  $\pm$ SD from n=3 experiments (145-161 cells per bar). **(D)** WHAMM<sup>HET</sup> and WHAMM<sup>KO</sup>  
995 MEFs were treated with rapamycin for 16h before being fixed and stained with LC3 or  
996 GABARAP antibodies (green) and DAPI (DNA; blue). Scale bars, 50 $\mu$ m, 25 $\mu$ m. The # of  
997 GABARAP puncta per cell was counted manually. Each bar represents the mean  $\pm$ SD from n=3  
998 experiments (30 cells per genotype per experiment). To calculate the puncta:cytoplasmic ratio  
999 of GABARAP fluorescence intensities, the mean fluorescence of GABARAP puncta was divided  
1000 by the mean cytoplasmic GABARAP fluorescence in ImageJ. Each bar represents the mean  
1001  $\pm$ SD from n=3 experiments (4-7 puncta per cell; 6-8 cells per genotype per experiment).  
1002 Significant p-values are noted (unpaired t-tests).

1003

1004 **Figure 6. WHAMM depletion disrupts LC3 and actin organization in proximal tubule cells.**

1005 **(A)** Human kidney proximal tubule (HK-2) cells were transfected with control siRNAs, GAPDH  
1006 siRNAs, or independent siRNAs targeting the WHAMM transcript before immunoblotting with  
1007 antibodies to WHAMM, tubulin, and GAPDH. **(B)** Transfected HK-2 cells were exposed to  
1008 media containing chloroquine for 6h before being fixed and stained with antibodies to LC3  
1009 (green) and actin (magenta). Scale bar, 10 $\mu$ m. **(C)** Lines were drawn through the magnified  
1010 images from (B) to measure pixel intensity profiles. Scale bar, 2 $\mu$ m.

1011

1012 **Figure 7. The Arp2/3 complex is crucial for autophagosome closure and actin**

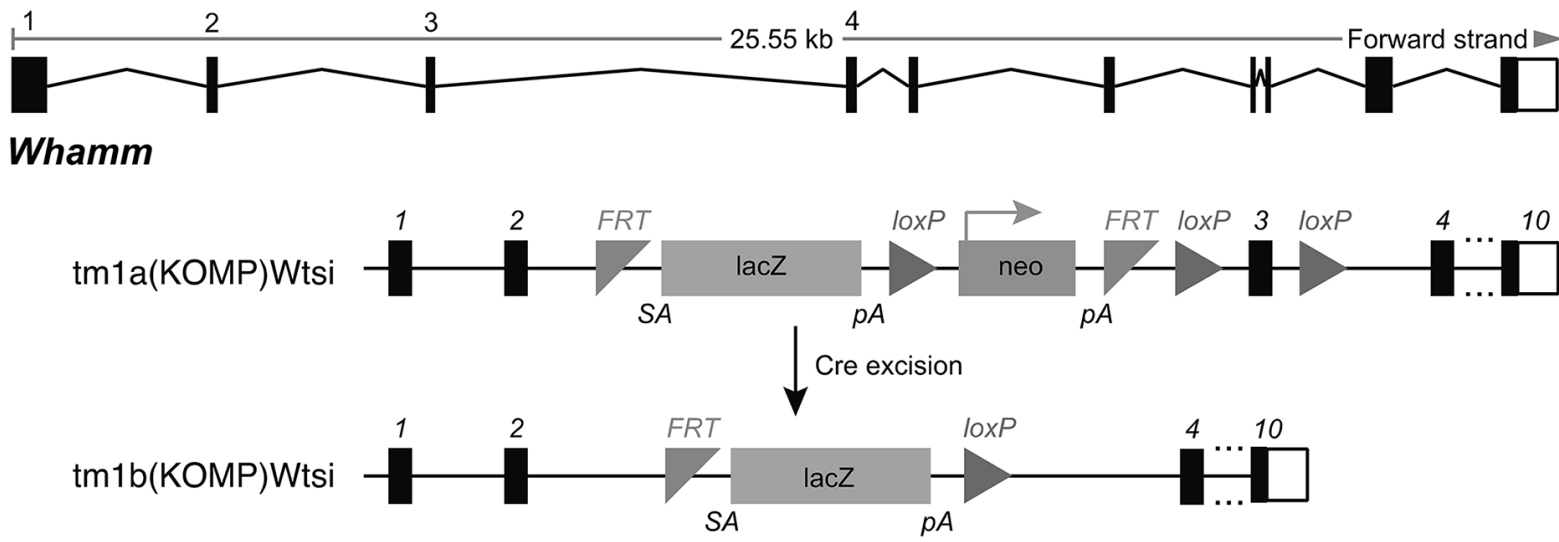
1013 **recruitment during selective autophagy. (A)** HK-2 cells were treated with normal media or

1014 media containing CK666 for 6h before being fixed and stained with LC3 antibodies. **(B)** Cells  
1015 were treated with chloroquine, or chloroquine plus CK666 for 6h before being fixed and stained  
1016 with antibodies to LC3 (green) and actin (magenta). **(C)** Lines were drawn through the images  
1017 in (B) to measure pixel intensity profiles. **(D)** The % of cells with LC3-positive rings and the # of  
1018 LC3-positive rings per cell were quantified. Each bar represents the mean  $\pm$ SD from n=3  
1019 experiments (150 cells per bar). **(E)** HK-2 cells were treated with chloroquine, or chloroquine  
1020 plus CK666 for 6h before being fixed and stained with STX17 antibodies (green), an LC3  
1021 antibody (magenta), and DAPI (DNA; blue). Scale bar, 20 $\mu$ m. Lines were drawn through  
1022 magnified images to measure pixel intensity profiles. **(F)** The % of cells with STX17-positive  
1023 vesicles and the # of STX17-positive vesicles per cell were quantified. Each bar represents the  
1024 mean  $\pm$ SD from n=3 experiments (230 cells per bar). **(G)** Cells were treated with media  
1025 containing chloroquine or chloroquine plus CK666 before being fixed and stained with  
1026 antibodies to LC3 (green) and p62 (magenta). Arrowheads highlight LC3-independent p62  
1027 structures. Lines were drawn through the images to measure pixel intensity profiles. Significant  
1028 p-values are noted (unpaired t-tests).

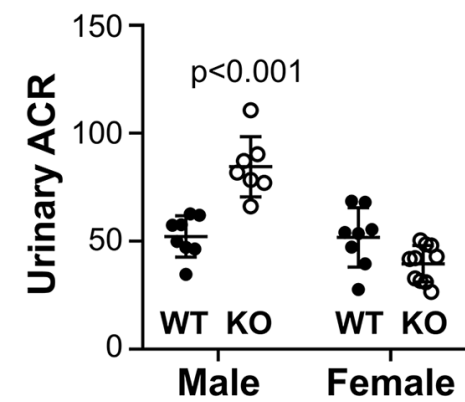
1029

1030 **Figure 8. WHAMM promotes Arp2/3 complex-mediated actin assembly during**  
1031 **autophagosomal membrane morphogenesis. (A)** HK-2 cells expressing LAP-WHAMM wild  
1032 type or a LAP-WHAMM W807A mutant deficient in Arp2/3 activation (both in green) were fixed  
1033 and stained with antibodies to LC3 (magenta) and actin (cyan). Scale bar, 10 $\mu$ m. **(B)** Model for  
1034 WHAMM and Arp2/3 complex function in autophagosome closure during cargo capture.  
1035 Aggregated protein cargo (gray) is ubiquitinated (green) prior to its engagement by autophagy  
1036 receptors like p62 (orange). WHAMM (purple) and the Arp2/3 complex (blue) promote the  
1037 assembly of actin filaments (red) necessary for autophagosome membrane morphogenesis. In  
1038 the absence of WHAMM or the Arp2/3 complex, actin assembly at autophagic membranes is  
1039 abrogated, resulting in inefficient receptor engagement and autophagosome closure.

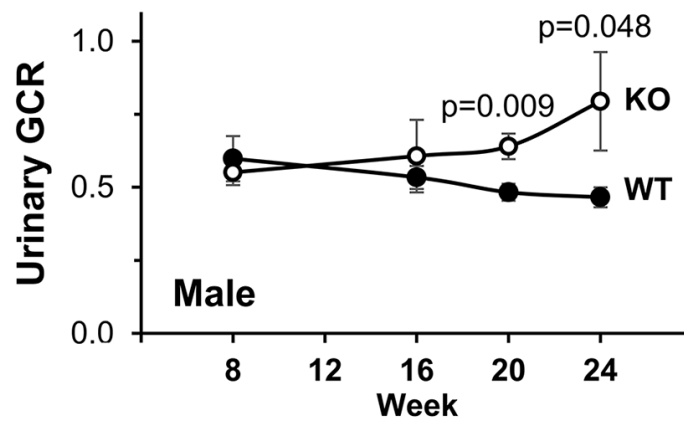
**A**



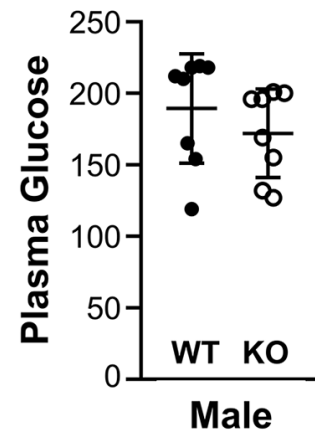
**B**



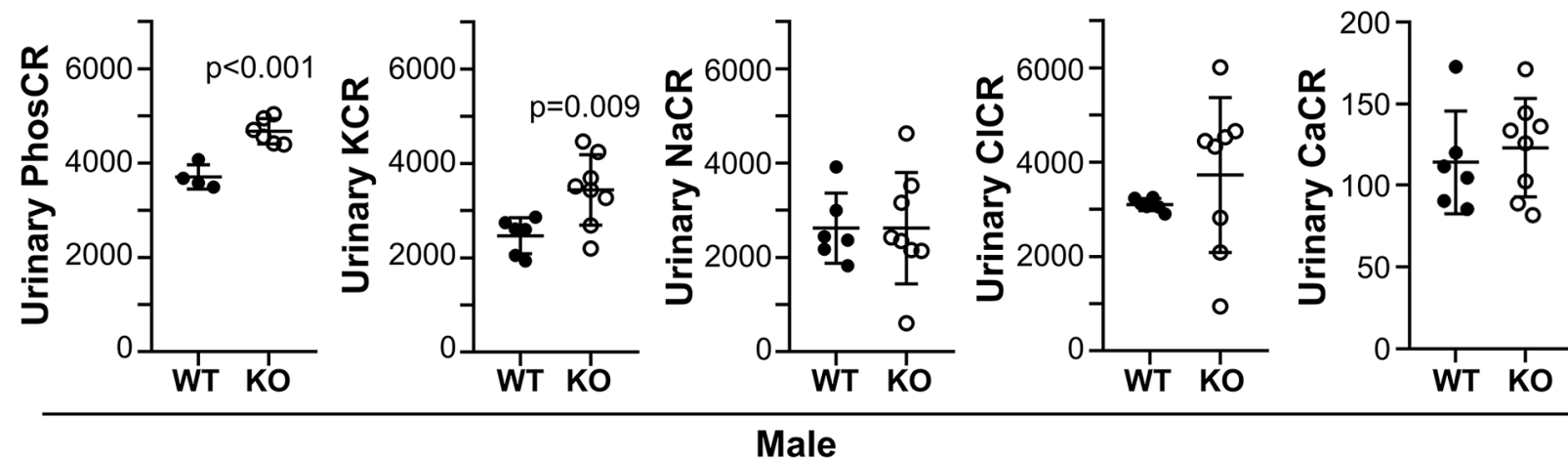
**C**

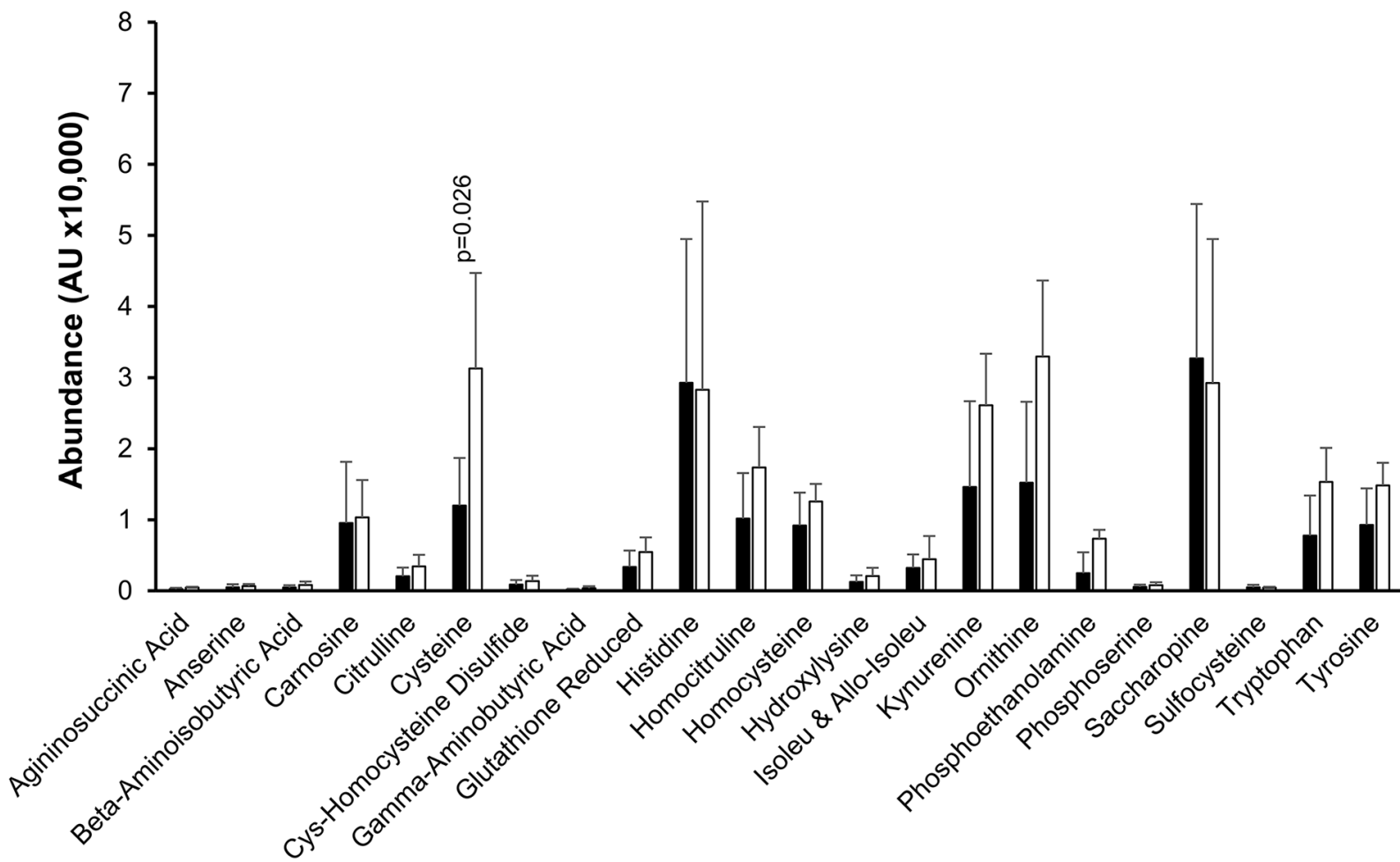
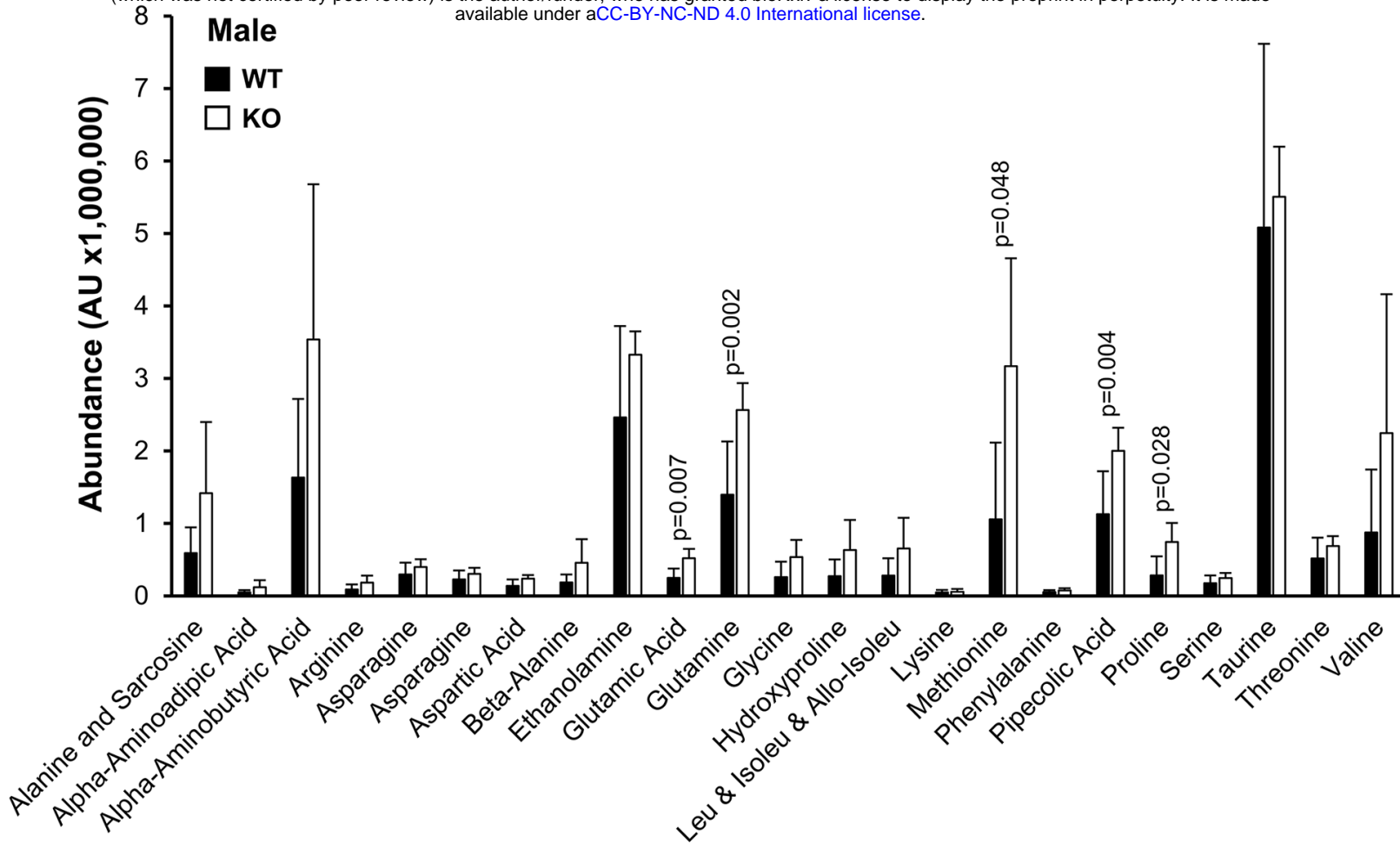


**D**

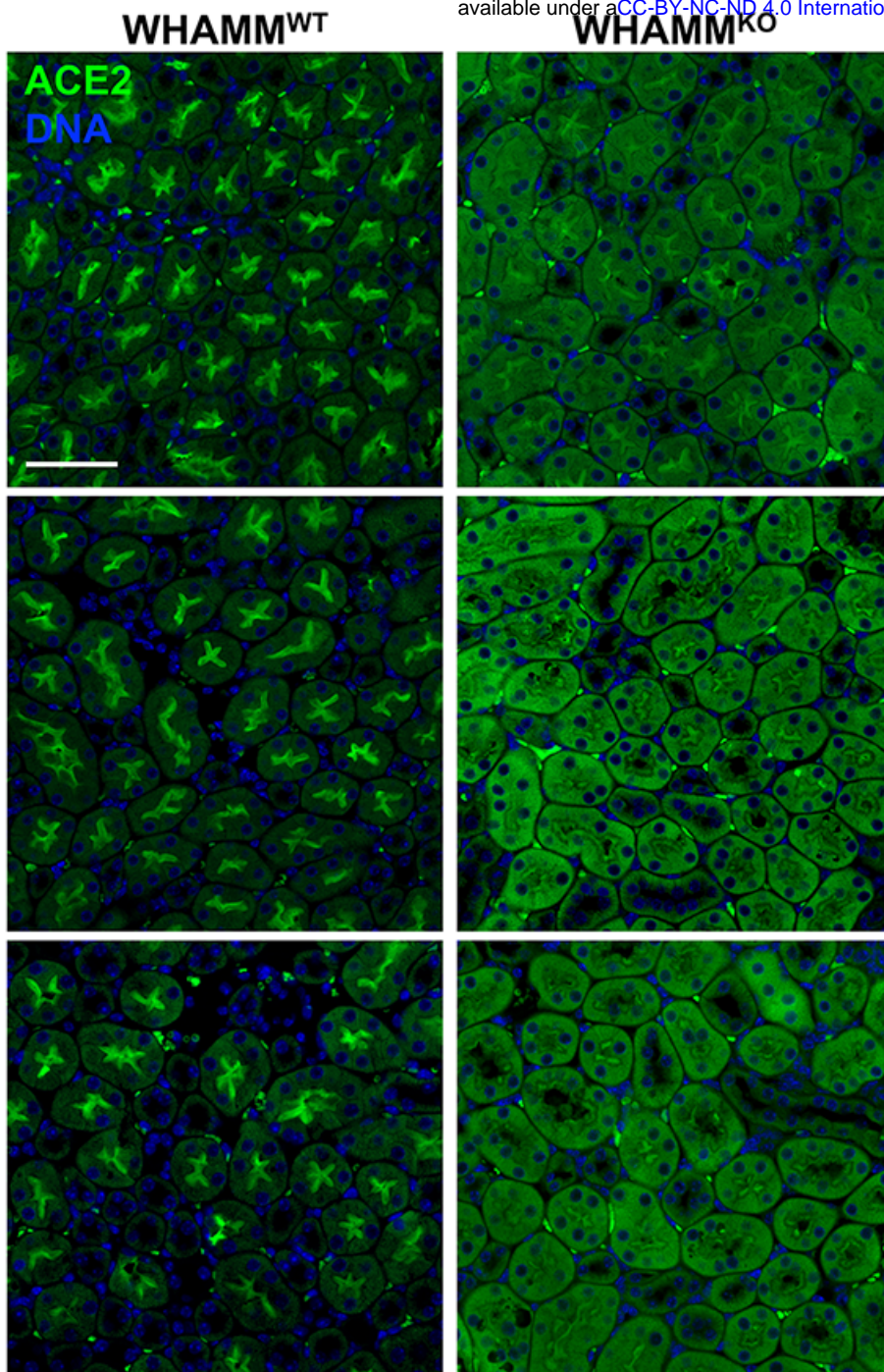


**E**

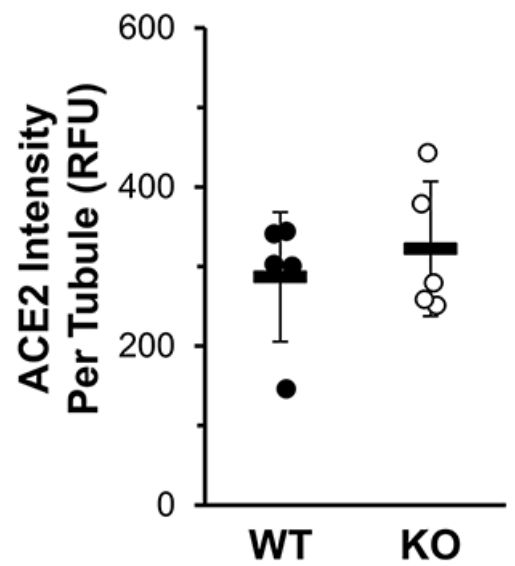




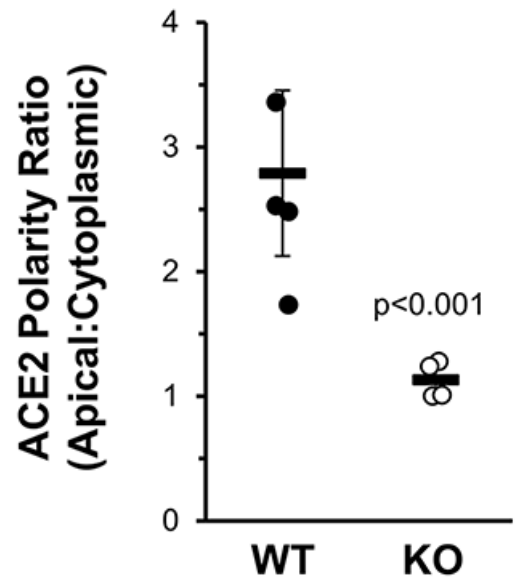
**A**



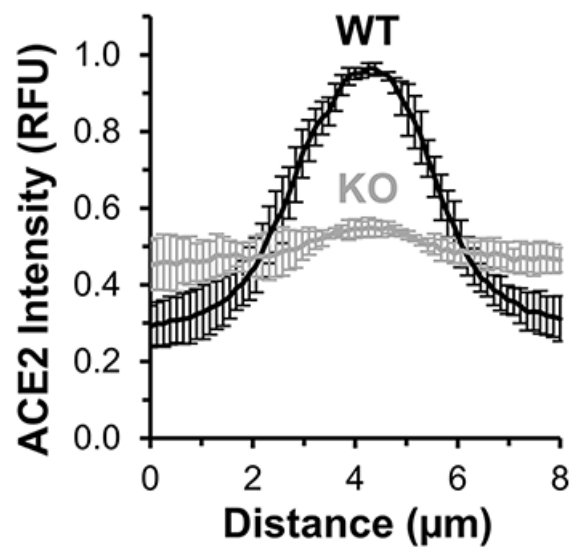
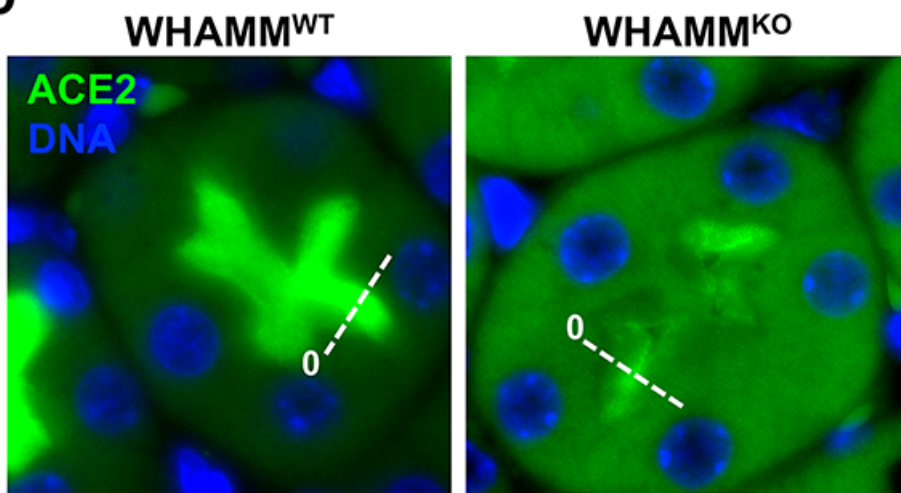
**B**



**C**

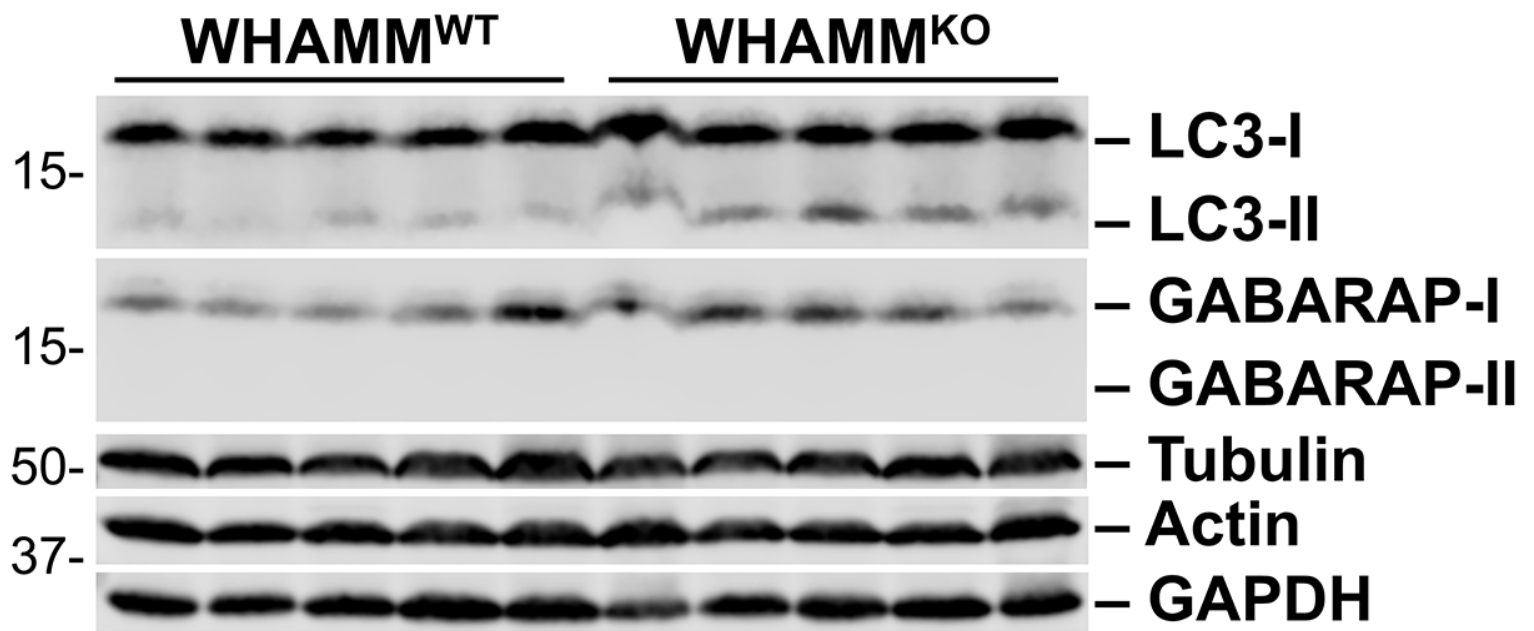


**D**

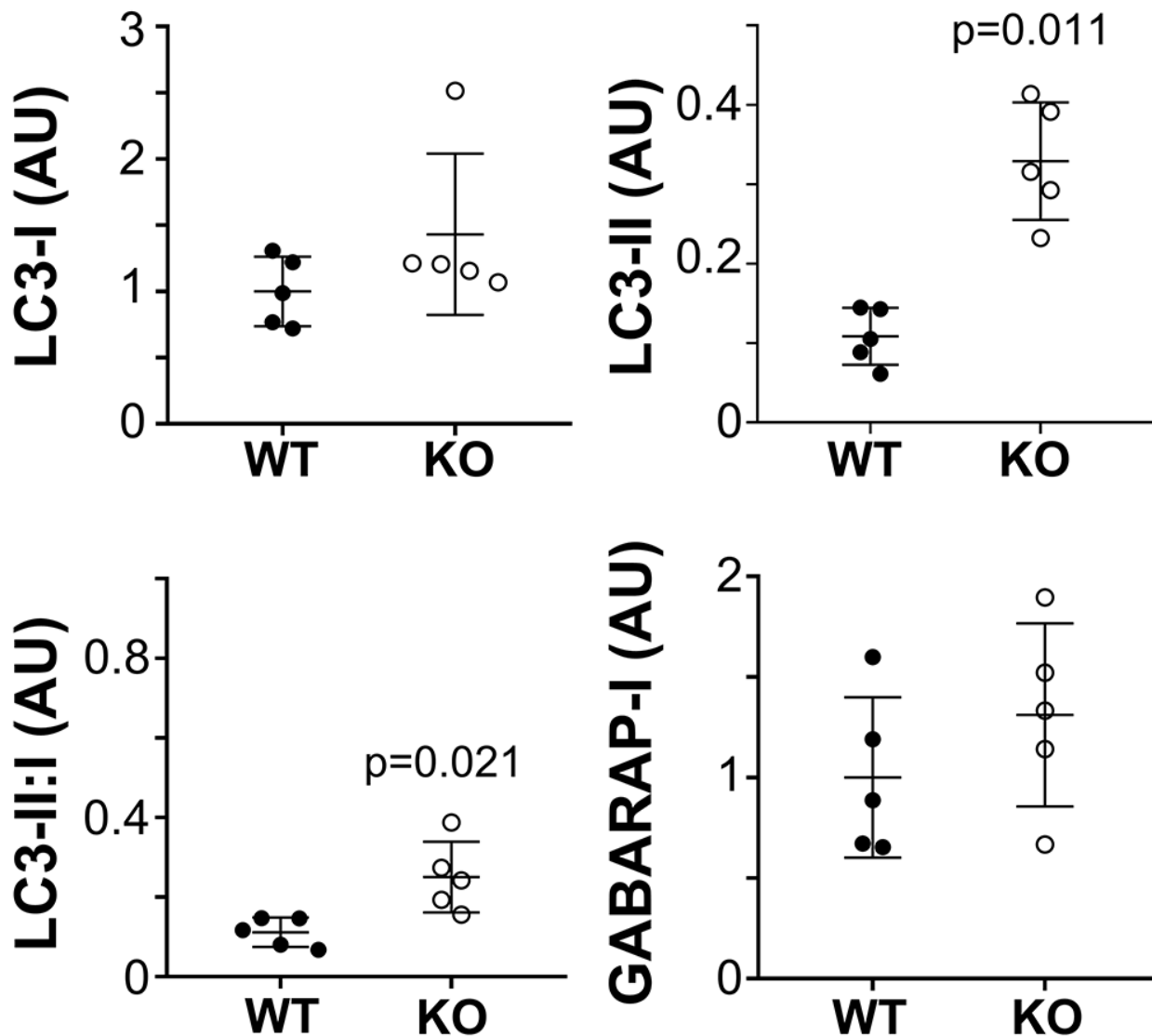




# A Male

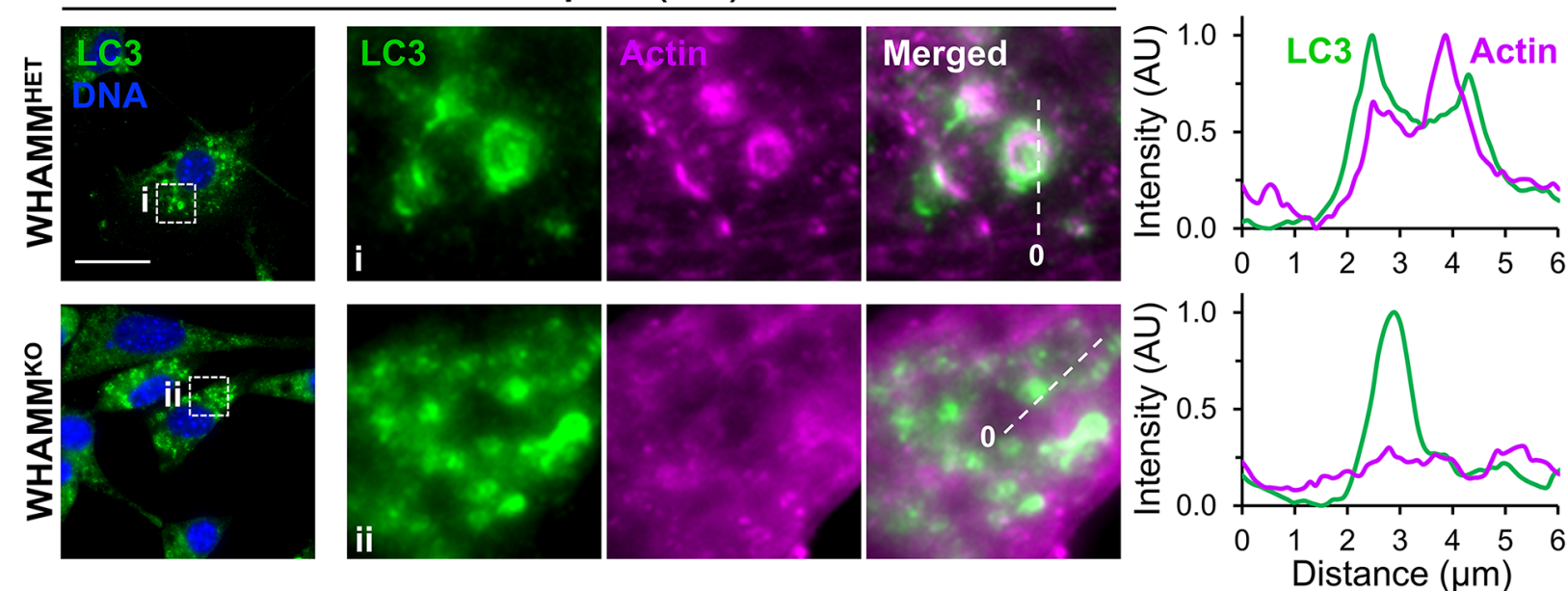


# B Male



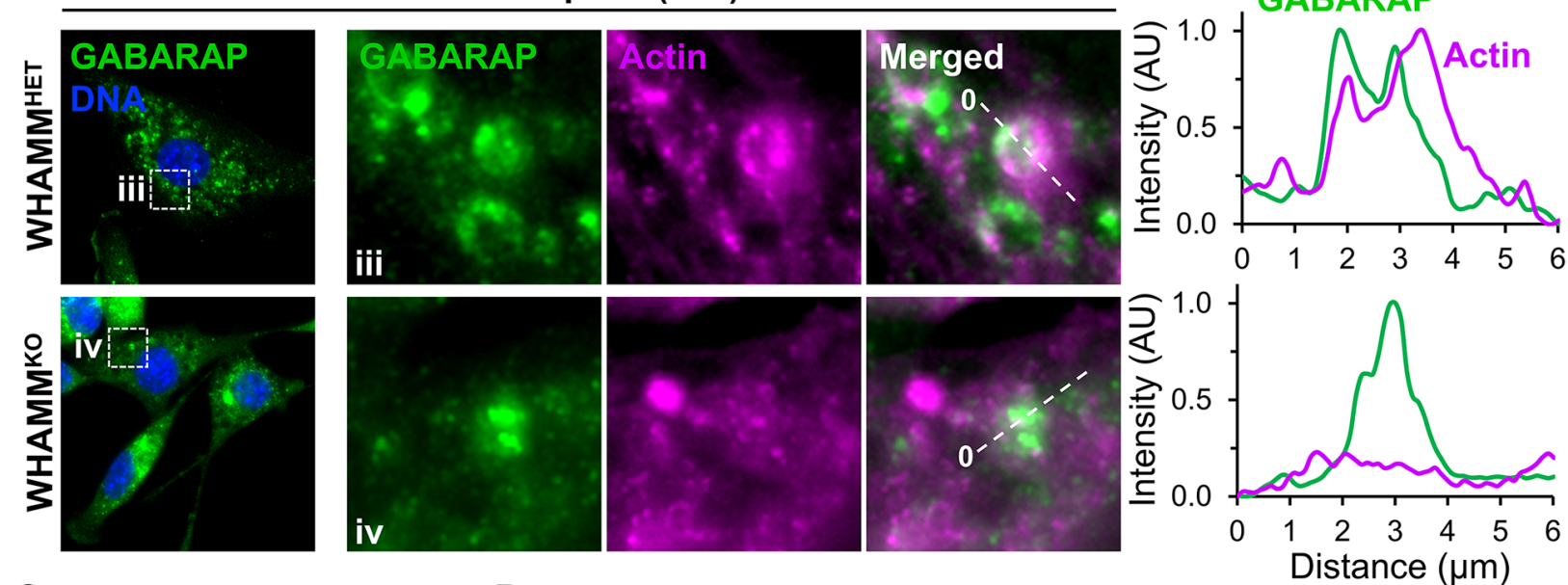
**A**

**Chloroquine (16h)**



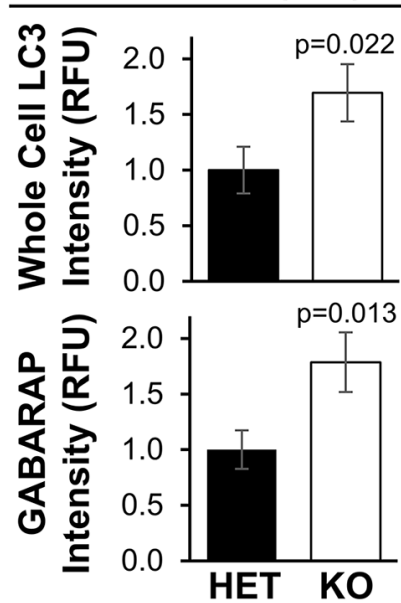
**B**

**Chloroquine (16h)**



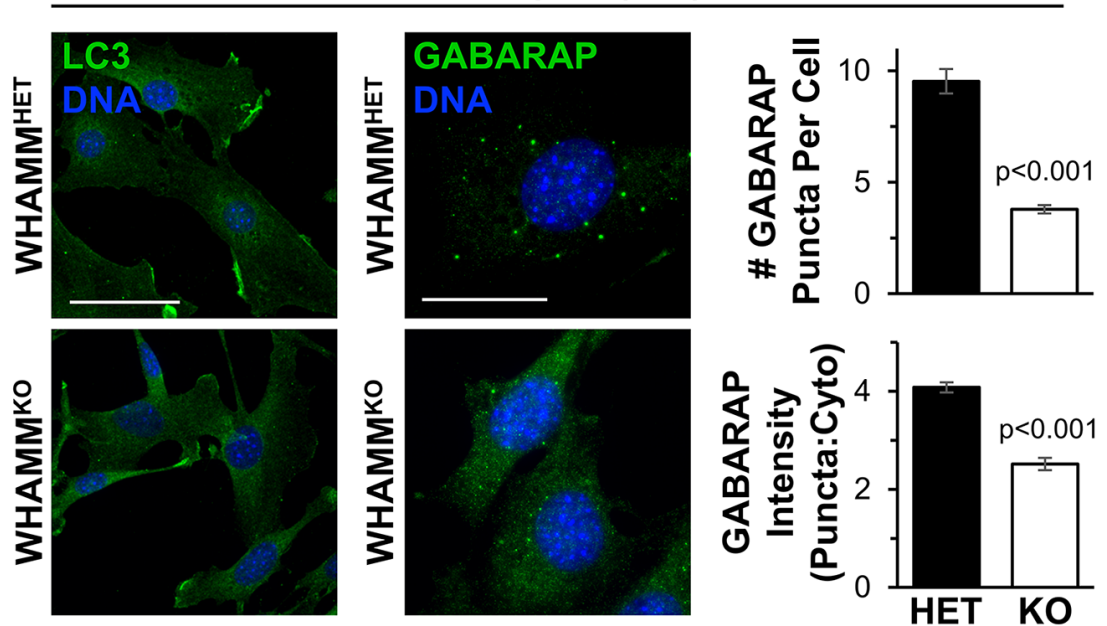
**C**

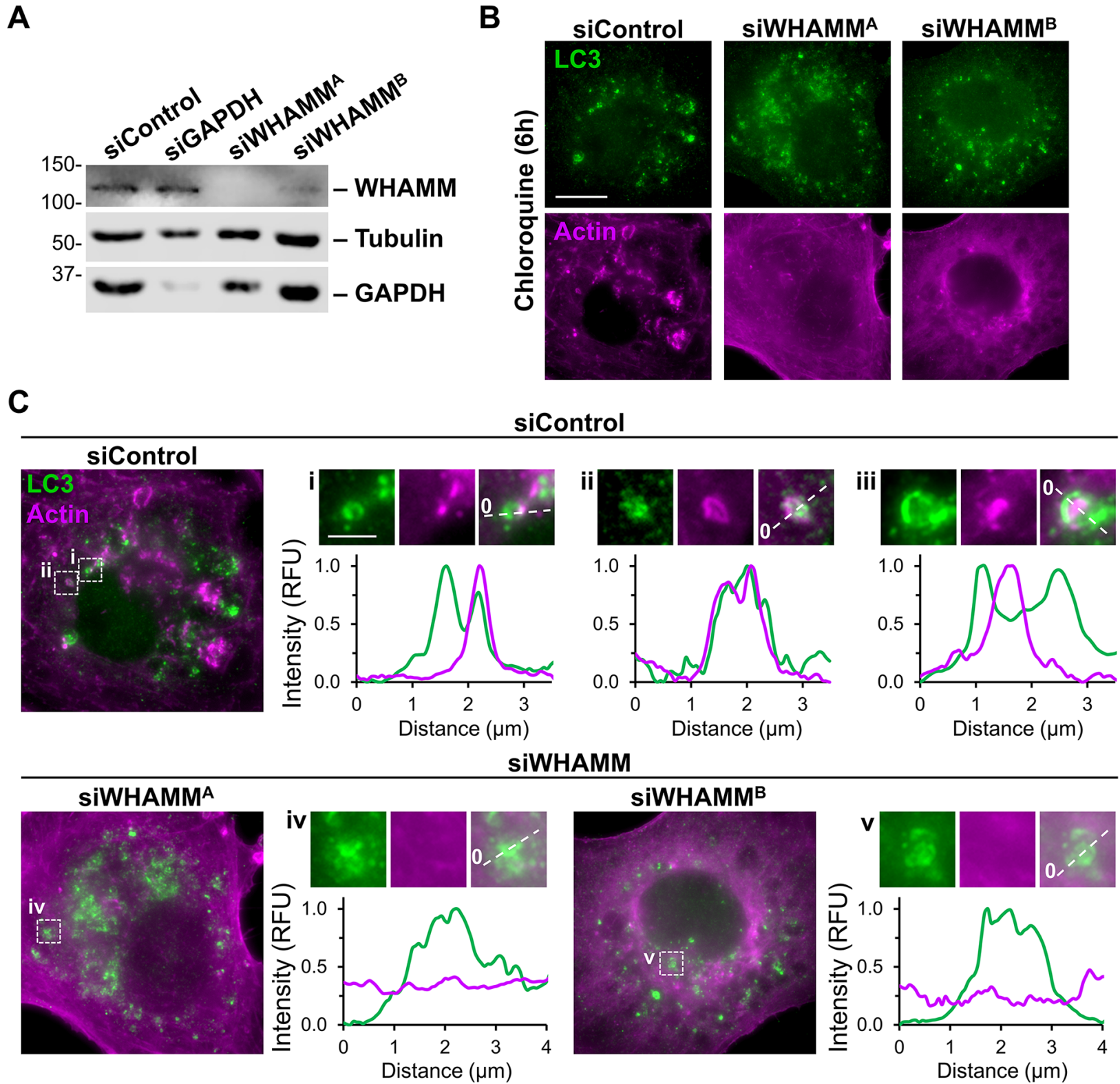
**Chloroquine (16h)**

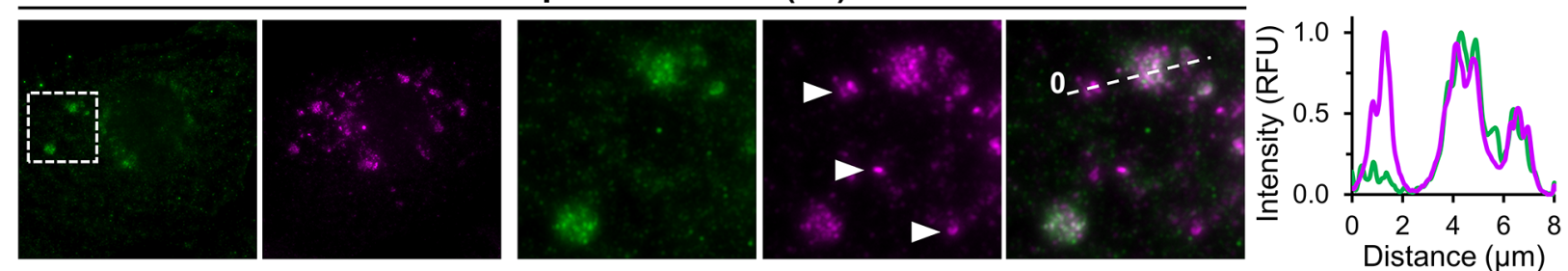
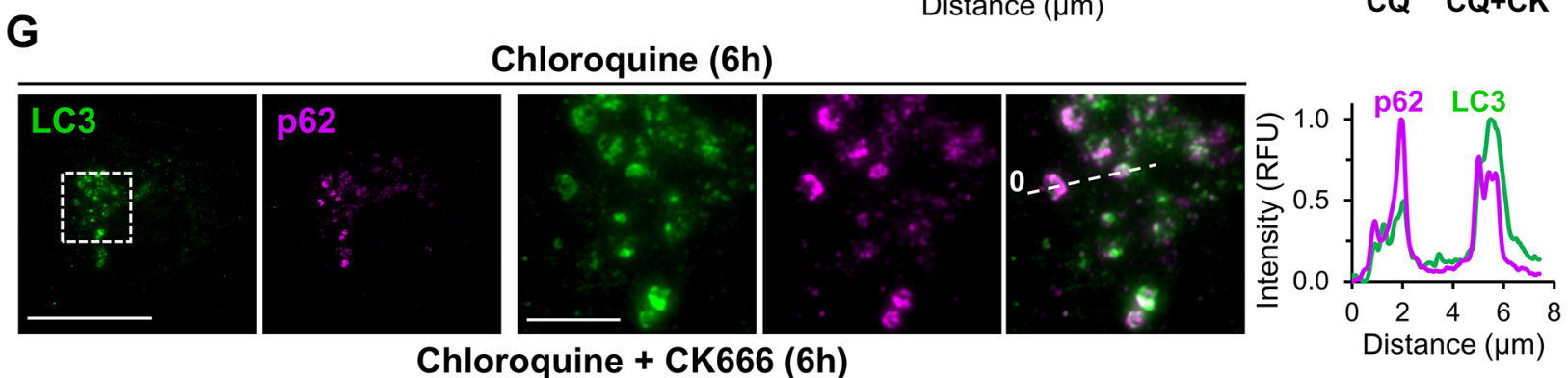
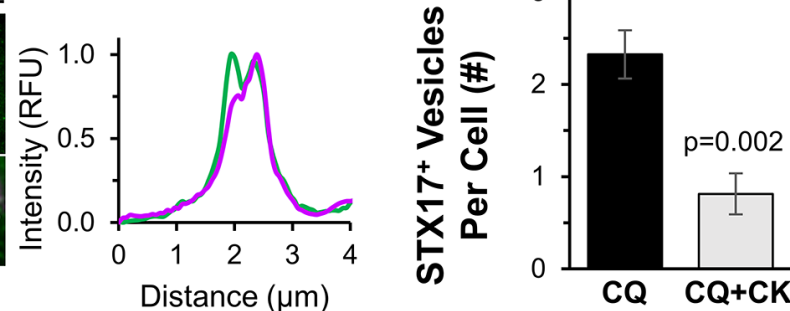
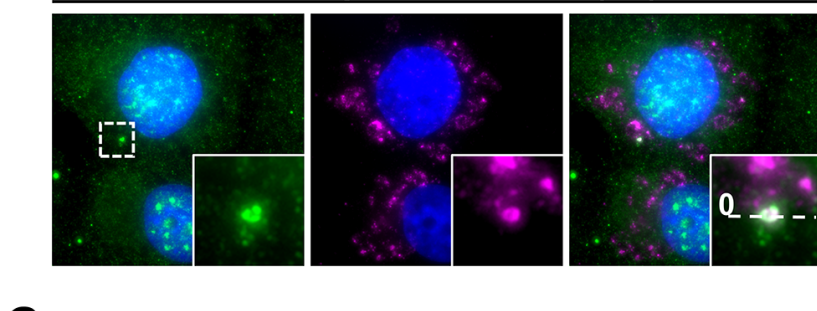
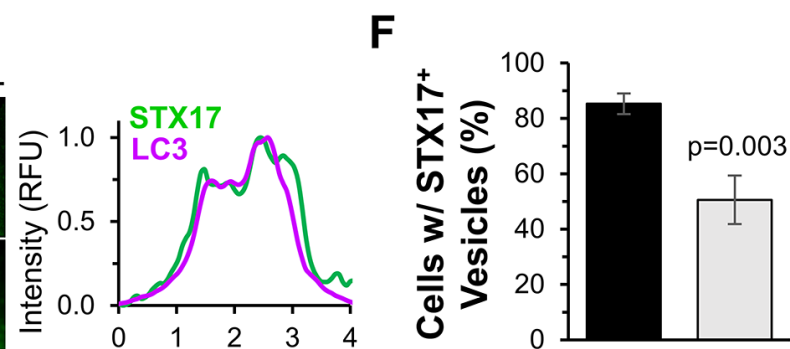
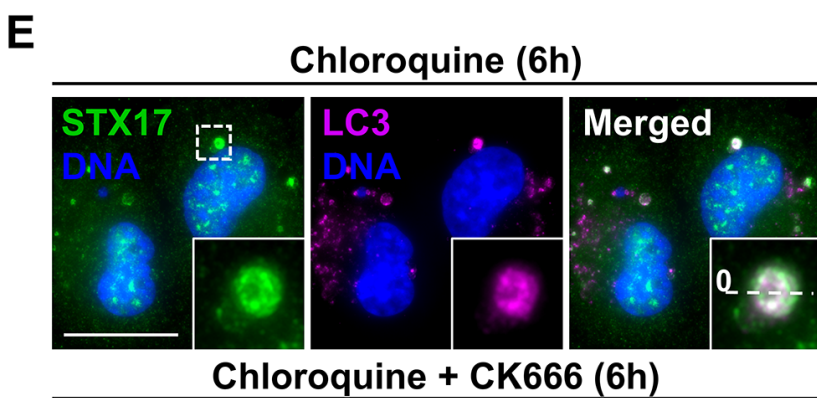
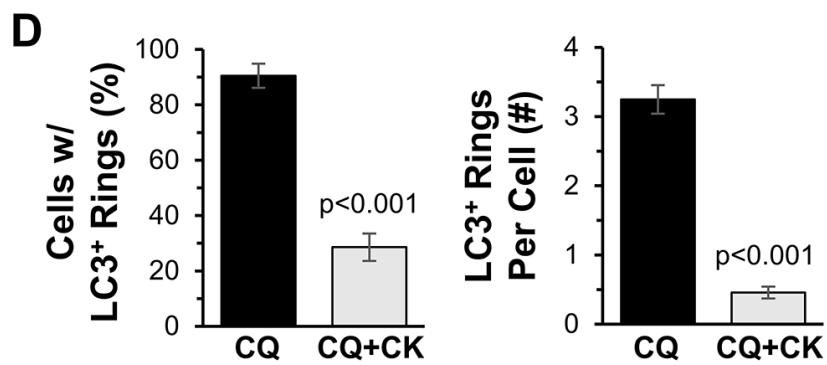
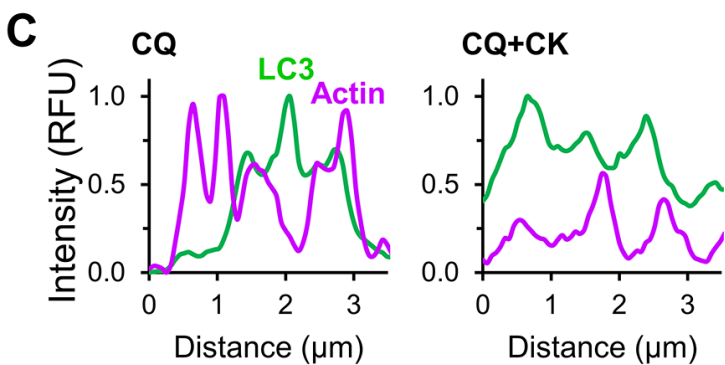
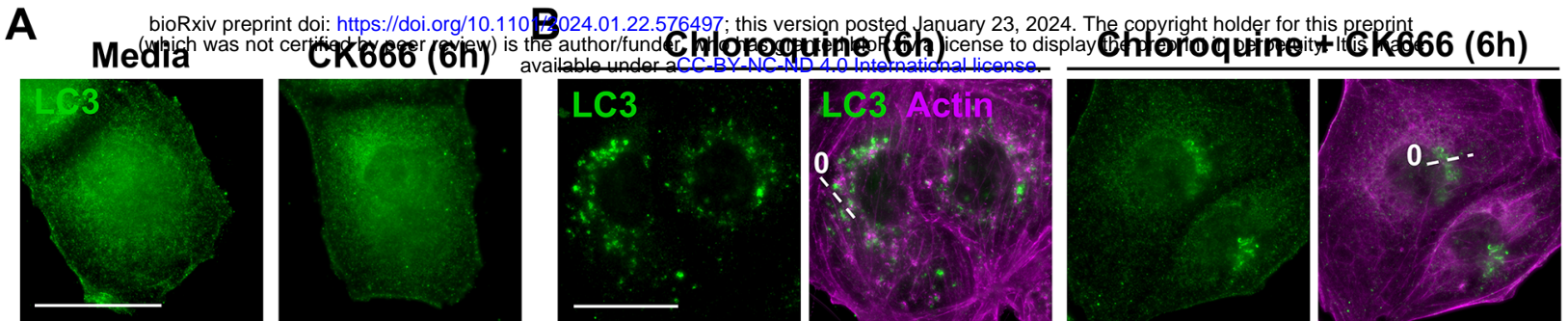


**D**

**Rapamycin (16h)**

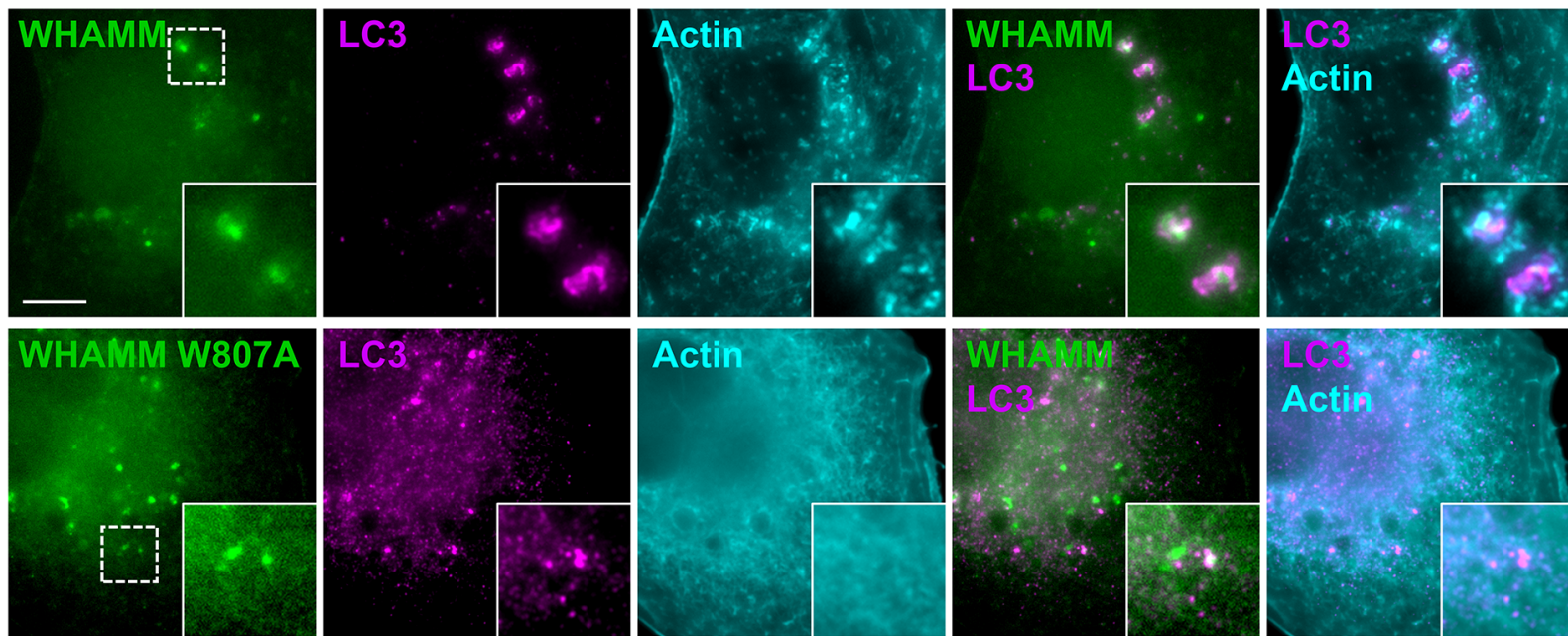






**A**

**Chloroquine (6h)**



**B**

**Cargo Capture & Autophagosome Maturation**

